

12-2016

Best Practices for Volume Flow Rate Measurements Using PIV at the Exit of a Turbulent Planar Jet

Rick Cressall
Utah State University

Follow this and additional works at: <https://digitalcommons.usu.edu/etd>



Part of the Mechanical Engineering Commons

Recommended Citation

Cressall, Rick, "Best Practices for Volume Flow Rate Measurements Using PIV at the Exit of a Turbulent Planar Jet" (2016). *All Graduate Theses and Dissertations*. 5218.
<https://digitalcommons.usu.edu/etd/5218>

This Thesis is brought to you for free and open access by the Graduate Studies at DigitalCommons@USU. It has been accepted for inclusion in All Graduate Theses and Dissertations by an authorized administrator of DigitalCommons@USU. For more information, please contact digitalcommons@usu.edu.



BEST PRACTICES FOR VOLUME FLOW RATE MEASUREMENTS USING PIV AT THE
EXIT OF A TURBULENT PLANAR JET

by

Rick Cressall

A thesis submitted in partial fulfillment
of the requirements for the degree

of

MASTER OF SCIENCE

in

Mechanical Engineering

Approved:

Barton Smith, Ph.D.
Major Professor

Ryan Berke, Ph.D.
Committee Member

Tadd Truscott, Ph.D.
Committee Member

Mark R. McLellan, Ph.D.
Vice President for Research and
Dean of the School of Graduate Studies

UTAH STATE UNIVERSITY
Logan, Utah

2016

Copyright © Rick Cressall 2016

All Rights Reserved

ABSTRACT

Best Practices for Volume Flow Rate Measurements Using PIV at the Exit of a Turbulent Planar Jet

by

Rick Cressall, Master of Science

Utah State University, 2016

Major Professor: Barton Smith, Ph.D.

Department: Mechanical and Aerospace Engineering

Particle image velocimetry (PIV) is used to make volume-flow-rate measurements at the exit of a turbulent, planar nozzle. The objective of this report is to assess a range of data acquisition and processing parameters. Data is acquired for volume flow rates of Reynolds numbers between 10,000 and 100,000 for both two-component (2C) and stereo PIV. The parameters are systematically changed one at a time and evaluated using differences in uncertainty, calculation time, and volume-flow-rate deviation. Data acquisition parameters follow the trends of previous work. A multitude of processing parameters were varied for several PIV processing methods. Recommendations for each method are developed and listed with potential drawbacks. 2C PIV was found to underestimate volume-flow-rate by 3-4% depending on the integration scheme and stereo PIV underestimated volume-flow-rate by 2%.

(79 pages)

PUBLIC ABSTRACT

Best Practices for Volume Flow Rate Measurements Using PIV at the Exit of a Turbulent Planar Jet

Rick Cressall

Particle image velocimetry (PIV) is an optical flow measurement technique that is used to measure flow at the exit of a turbulent, rectangular nozzle. The objective of this report is to determine how to best make this measurement. The quality of the measurement is affected by a range of data acquisition and how data are processed. Measurements are made over a range of different flows using the two main types of PIV: 2C and stereo. Previous work done for data acquisition of PIV in general is found to apply. Different processing options are systematically examined using several different metrics. Recommendations for each are developed and listed with potential drawbacks. 2C PIV was found to slightly underestimate flow by 2-3% depending on how several different measurements are joined. Stereo PIV underestimated flow by 2%.

For the insurgent team that installed the bomb that blew up right next to me. If one of you hadn't messed it up somehow, the entire thing would have gone off rather than *just* the initiation charge. And also to the entrance counselor who, when I told you I wanted to be an engineer, looked at my math placement score and told me how good the business school was.

ACKNOWLEDGMENTS

Thanks to BJ Williams, Robbie Schaap, and Austin Parker for the help and the distractions. Thanks to Dr. Alex Mychkovsky, Bechtel Marine Propulsion, and Bettis Atomic Power Laboratory for both funding my research and providing invaluable feedback. Finally thanks to my adviser, Dr. Barton Smith, for looking out for my best interests, academic and otherwise.

Rick Cressall

CONTENTS

	Page
ABSTRACT	iii
PUBLIC ABSTRACT	iv
ACKNOWLEDGMENTS	vi
LIST OF TABLES	ix
LIST OF FIGURES	x
1 Introduction	1
2 Background	2
2.1 Volume-Flow-Rate	2
2.2 Characteristics of a Jet	2
2.3 Particle Image Velocimetry	3
2.3.1 Data Acquisition Parameters	5
2.3.2 Processing Algorithm	6
2.4 Measuring Volume-Flow-Rate	9
2.4.1 2C PIV	9
2.4.2 Stereo PIV	10
2.4.3 Calculating Volume-Flow-Rate	12
2.4.4 Volume-Flow-Rate Uncertainty	12
2.4.5 Metrics	15
3 Equipment	18
3.1 Test Facility	18
3.2 Flow Meter	19
3.3 Nozzle	20
3.4 Camera	21
3.5 Optics	22
3.6 Laser	22
3.7 Calibration Plate for Stereo PIV	23
3.8 Stereo PIV Setup	24
3.9 Facility Operation	25
3.9.1 Flow Control	25
3.9.2 Particle Seeding	26

4	Results	31
4.1	Facility Shakedown	31
4.2	Processing	36
4.2.1	Processing Recommendations	45
4.3	PIV Data Acquisition Parameters	47
4.3.1	Data Acquisition Recommendations	48
4.4	Volume-Flow-Rate Measurements	50
4.4.1	Volume-Flow-Rate From 2C PIV	51
4.4.2	Volume-Flow-Rate From Stereo PIV	52
5	Conclusions	55
	REFERENCES	56
	APPENDICES	58
A	Processing Parameters	59

LIST OF TABLES

Table	Page
4.1 Data acquisition locations for facility shakedown.	31
4.2 Reference list of processing parameters giving a short description of what parameter is varied.	37
4.3 Results of volume-flow-rate measurements using 2C PIV. Negative values indicate measurements made by PIV were less than the flow meter. Values in parentheses are adjusted for nozzle leak.	52
4.4 Results of volume-flow-rate measurements made using stereo PIV. Negative values indicate measurements made by PIV were less than the flow meter.	52

LIST OF FIGURES

Figure	Page
2.1 Cross correlation map of two IW's. The location of the peak indicates the most probable particle displacement.	4
2.2 Nozzle coordinate system.	9
2.3 2C PIV setup for measuring volume-flow-rate. Measurement locations for 2C PIV are shown as a velocity profile illuminated by a laser sheet. Several example locations are shown.	10
2.4 Side view of a planar nozzle for stereo PIV measurements. The Gaussian nature of the laser sheet covering the exit plane limits how close it can be placed. Arrow outside of the nozzle show fluid being entrained inside of the measurement plane. This increases the volume-flow-rate of the measured flow.	11
2.5 A common stereo PIV calibration error occurs when the calibration plane and the measurement plane do not perfectly align. A shift of the calibration plane towards the cameras will cause the same particle to appear in two different locations.	11
2.6 Mean velocity field for Reynolds number = 100,000 at the $z = 0.00$ location. Boxed locations identify where uncertainty was taken to represent the core and shear flow regions.	16
3.1 Test facility used to acquire data. Flow circulates in a clock-wise direction.	18
3.2 Side-view schematic of test facility used to acquire data. Flow circulates in a clock-wise direction.	19
3.3 Top-view schematic of test facility used to acquire data. Flow is driven from left to right.	20
3.4 High aspect ratio, rectangular nozzle used to acquire data.	21
3.5 Side view schematic of nozzle used to acquire data. Flow is driven from left to right.	22
3.6 Top down view schematic of nozzle used to acquire data. Flow is driven from left to right.	23
3.7 As built, internal dimensions of the nozzle at the exit plane.	23
3.8 Calibration plate used for stereo PIV measurements.	24

3.9	Top down schematic of the facility. Subfigure (a) shows how large changes in the index of refraction at the air-water boundary cause optical distortion. Subfigure (b) shows how Plexiglas prisms mounted to the facility reduce the angle of incidence at the air-water boundary. Shaded areas represent locations filled with water.	25
3.10	View of the calibration plate without a water filled prism to correct for index of refraction changes.	26
3.11	View of the calibration plate with a water filled prism to correct for index of refraction changes.	27
3.12	Viscosity of water as a function of temperature.	28
3.13	Raw particle image for 2C PIV. The nozzle occupies the upper left and lower left portion of image. Particles that appear inside of the nozzle are caused by light reflecting off particles.	29
3.14	Raw particle image for stereo PIV.	30
4.1	Nozzle and laser sheet orientation. Subfigure (a) shows coordinate system centered at the exit plane. Subfigure (b) shows the orientation of the laser sheet for 2C PIV in the x - y plane. The laser sheet is shown as a green plane illuminating a velocity profile. Subfigure (c) shows the orientation for 2C PIV in the x - z plane. Subfigure (d) shows the orientation for Stereo PIV where velocity is measured over the exit plane of the nozzle.	32
4.2	Velocity profiles taken at the nozzle exit for $Re = 10,000$. Subfigure (a) shows average (\bar{u}) velocity profiles in the x - y plane. Subfigure (b) shows average (\bar{u}) velocity profiles in the x - z plane.	33
4.3	Average velocity profiles (\bar{u}) taken at the nozzle exit for $Re = 100,000$. Subfigure (a) shows velocity profiles in the x - y plane. Subfigure (b) show velocity profiles in the x - z plane.	34
4.4	Developing flow can be seen in cross stream velocity profiles near the edges of the nozzle in the x - y profile at $z = 53.5$ (a) and x - y profile at $y = 3.8$ (b) for flow at $Re = 100,000$	35
4.5	Cross section view of nozzle illustrating a 2C PIV setup. To maintain a similar FOV between measurement planes, differences in the index of refraction mean the ratio of camera movement (dz_c) to laser movement (dz_l) are not 1:1.	36
4.6	Increases of random uncertainty for each processing case. Uncertainty is shown as a relative increase from BC processing (P0001). Absolute uncertainty in the shear is larger than uncertainty in the core.	38

4.7	Calculation time of each processing case. Calculation time is shown as a relative increase over the calculation time of BC processing (P0001).	39
4.8	Volume-flow-rate deviation from the BC for each processing case. Deviation is determined by the absolute difference in volume-flow-rate.	40
4.9	Velocity profiles for all of the CPU processed cases. Only the case processed using the high-accuracy final pass option and the BC processing are in color to illustrate the velocity bias.	41
4.10	Random uncertainty of the mean and random instantaneous uncertainty of the baseline processing case, P0002 and the processing case for adaptive IW, P0008. Data in black is the random uncertainty of the mean from Fig. 4.6.	42
4.11	Random instantaneous uncertainty, in blue, plotted with the random uncertainty of the mean from Fig. 4.11 for selected processing cases.	43
4.12	Random uncertainty increase versus calculation time. The lower right portion of the figure is the ideal location representing low uncertainty and fast calculation time. .	44
4.13	Volume-flow-rate deviation and calculation time. The ideal location of the figure is the lower right portion indicating a volume-flow-rate close to the BC processing and fast calculation time.	45
4.14	Random uncertainty of the velocity mean versus particle displacement. A larger particle displacement results in a larger dynamic velocity range, which decreases instantaneous random uncertainty. Result at a particle displacement of 10 pixels is from the baseline processing case P0002.	47
4.15	Volume-flow-rate deviation versus particle displacement. Larger particle displacements result in a larger velocity dynamic range. Result at a particle displacement of 10 pixels is from the baseline processing case P0002.	48
4.16	Random uncertainty versus particle density. The probability of a valid vector increases with particle density, with diminishing returns after 8 particles in each IW. Results closest to 11 particles per IW is from baseline processing case P0002. . .	49
4.17	Volume-flow-rate deviation versus particle density. Insufficient particle density increases volume-flow-rate deviation. Result closest to 11 particles per IW is from baseline processing case P0002.	49
4.18	Location of the leak. Water may be moving around the outside of the nozzle and the nozzle adapter plate. This flow is measured by the flow meter but not PIV measurements.	50

4.19 Locations of profiles in the x - y plane that are used to calculate volume-flow-rate. Vertical green bars are representative of the location of each measurement plane and thickness of the laser sheet. They are plotted over a velocity profile for $Re =$ $10,000$ in the x - z plane. The profile data are from shakedown. A limited number of measurement planes are used to represent the entire profile, with each containing information only from the measurement plane. Information about the flow between measurement planes is interpolated using information from the two bounding mea- surement planes. Integration using the trapezoid rule assigns equal weight to each of the bounding measurement planes.	53
4.20 Average streamwise velocity of a Stereo PIV measurement at $Re = 100,000$	54

CHAPTER 1

Introduction

Planar, or rectangular nozzles are often used in engineering applications of flow handling for their ease of manufacture and well characterized behavior. Knowledge of volume-flow-rate is important for validation of numerical models. Volume flow measurements at the exit of the nozzle are complicated by several factors. Fluid exiting the nozzle into a stationary fluid will initially have a velocity profile resembling a top-hat. At the edges of the jet, at the boundary between the fast and slow moving fluids, friction transfers momentum from the jet to the stagnant fluid adjacent to the jet. This increases the amount of fluid in the jet and increases the volume flow. This effect increases the farther downstream of the nozzle exit measurements are acquired. For better accuracy, measurements should be acquired as close to the nozzle exit as possible. However, it is not possible to make measurement exactly at the exit.

Particle Image Velocimetry (PIV) is an optical imaging flow measurement technique that provides near instantaneous two or three-dimensional velocity fields. The accuracy of PIV is influenced by a multitude of data acquisition and processing parameters. While not always the case, data acquisition parameters can generally be controlled. There are also many different processing schemes, each with their own subset of options, that produce velocity fields of varying quality. Additionally, the processing time between different schemes vary by several orders of magnitude.

While PIV is often used to characterize flow fields, to the best of our knowledge, there has been no attempt to ascertain its accuracy for measuring volume-flow-rate. Work performed by van Doorne and Westerweel [1] use PIV to measure flow in a pipe while measuring volume-flow-rate, but only use it to verify the mean velocity of the flow as determined through PIV.

To develop a list of best practices, this thesis measures volume flow rates through a well characterized nozzle. The effects of data acquisition and processing parameters will be investigated by determining a baseline measurement and varying a single parameter at a time. Each parameter will be compared using several metrics that will include: accuracy, uncertainty, and processing time.

CHAPTER 2

Background

2.1 Volume-Flow-Rate

Volume-flow-rate through a nozzle is

$$Q = \int_{A_c} u \, dA_c \quad (2.1)$$

where A_c is the area of the exit plane and u is the local streamwise velocity. Particle Image Velocimetry (PIV) determines the flow field on a regularly spaced grid. Eq 2.1 is modified to be

$$Q \approx \sum_{j=1}^{N_z} \sum_{i=1}^{N_y} \bar{u}_{i,j} \Delta y \Delta z \quad (2.2)$$

where \bar{u} represents the time-mean velocity at each location and $\Delta y \Delta z$ represent the area that each velocity vector represents.

2.2 Characteristics of a Jet

Turbulent jets are a type of free shear flow where the name “free” implies the flow is removed from walls and turbulence occurs because of the mean-velocity gradients [2]. Fluid exits a nozzle with a near flat-topped velocity profile into a quiescent fluid. The jet can be divided into two regions, the core and the shear layer. The core makes up the top of the flat-topped velocity profile and is not influenced by the surrounding quiescent fluid. The shear layer is the interface between the core and the quiescent fluid characterized by a sharp velocity gradient.

In the shear layer, momentum is transferred from the fast moving fluid to the quiescent fluid. Momentum remains constant in the downstream direction and is determined by

$$M = \int_{A_c} \left(u^2 + \overline{u' u'} + \frac{p_s}{\rho} \right) dA_c \quad (2.3)$$

where p_s is the gage static pressure and $\overline{u'u'}$ is the Reynolds stress. Both $\overline{u'u'}$ and p_s/ρ are smaller than the u^2 term, have opposite signs, and are generally ignored [3]. Reynolds stress is a measure of the mean fluctuations about the average velocity in turbulent flow. The result of momentum transfer is that fluid is entrained into the jet and increases the volume-flow-rate.

2.3 Particle Image Velocimetry

Particle Image Velocimetry (PIV) is a, non-intrusive, optical flow measurement technique that determines velocity vector fields. A laser sheet is used to illuminate tracer particles which are imaged twice, with a small but known Δt . The images are subdivided into small interrogation windows (IW). The most probable displacement for the particles inside each IW is determined in pixels. Velocity can then be determined by using a mapping function to convert camera pixels to physical space.

Two component (2C) PIV passes a laser beam through spherical and cylindrical optics to create a laser sheet which forms a measurement volume. A camera is positioned orthogonal to the laser sheet and captures two components of velocity. This setup cannot determine the through plane motion of particles. Stereo PIV is an extension of 2C PIV that uses a second camera. Cameras are positioned with different viewing angles and allows the third velocity component to be extracted. This requires both cameras to be focused on the same position in the flow and a more involved calibration [4].

PIV does not determine velocity by tracking the movement of individual particles, but uses a cross correlation to determine the most probable displacement of particles in an IW. The formula for a cross correlation is

$$C(x, y) = \sum_{i=-K}^{K} \sum_{j=-L}^{L} I(i, j) I'(i + x, j + y). \quad (2.4)$$

The pixel intensity values of each IW are given by I and I' . K and L are typically $1/2$ of the IW size. Increasing the values of K and L increases the range of particle displacement detection. Each combination of x and y are a potential displacement of the particles inside of the IW between images. Ideally, the value of $C(x, y)$ is a maximum when the x, y values match the actual particle

displacement. The location of the peak indicates the most probable particle displacement. Figure 2.1 shows a correlation map with a single peak. The size of the peak is only important in distinguishing it from noise. As this is a statistical method, spurious velocity vectors occur and must be removed in a post-processing step [5]. The cross correlation map can also be determined by exploiting properties of the convolution theorem and Fast Fourier Transform [6].

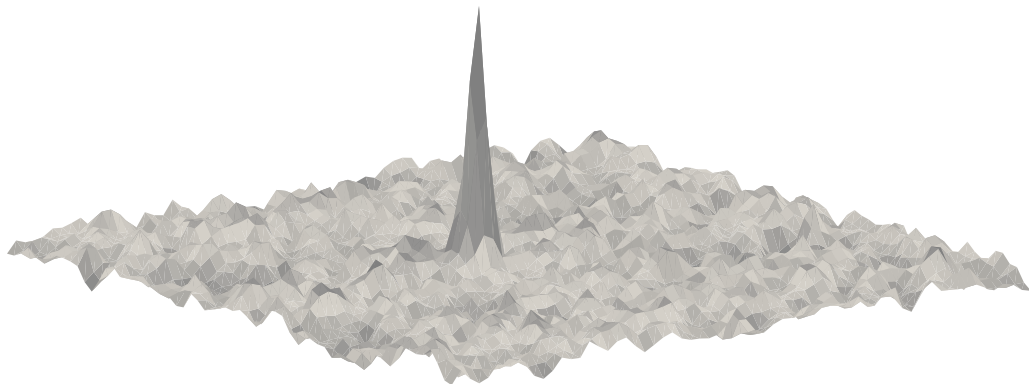


Fig. 2.1: Cross correlation map of two IW's. The location of the peak indicates the most probable particle displacement.

Each IW produces a single vector in the vector field. Spacial resolution can be increased by overlapping IWs or by making them smaller. The minimum size of an IW has two primary limitations. First, sufficient particles must be present so that the strength of the cross-correlation peak can be clearly distinguished from noise. Keane and Adrian [7] have shown that having 8 particles per IW is sufficient to ensure a 95% valid detection rate. Second, particle displacement must be less than the IW size, generally limited to $1/4$ of its size. This prevents particles from moving far enough that they are not present in both IWs.

An iterative multipass scheme is often used. Each pass produces a vector field that is used as a predictor for the next pass with the following step refining the measurement. After the first pass, this removes the limitation of particle displacement and IW size. This allows a higher spacial resolution by starting with a large IW size and reducing it on subsequent passes.

2.3.1 Data Acquisition Parameters

There are several data acquisition parameters that influence the quality of data collected. Guidelines for the following data acquisition parameters are taken from Adrian [5] and apply to both 2C and stereo PIV.

Choosing a proper depth of field for PIV images allows all particles within the measurement volume of the laser sheet to be in focus. Depth of field is a function of the relative lens aperture ($f^\#$), image magnification (M_O), and the wavelength of the laser (λ) and determined by

$$\delta_z \approx 4 \left(1 + \frac{1}{M_O} \right)^2 f^{\#2} \lambda. \quad (2.5)$$

Image magnification is the ratio of the camera sensor size to the Field Of View (FOV) size. Adrian [5] recommends a minimal magnification to avoid bias errors given by

$$M_{min} = \frac{2d_r}{\left(1.5\delta_z \lambda + d_p^2 \right)^{1/2}} \quad (2.6)$$

for a given focal depth of field. This is the smallest magnification that avoids bias errors, due to the finite resolution of the recording medium.

Particle image size (d_τ) is the size, in pixels of particles imaged by the camera. It is determined by a combination of the magnified particle diameter, the diffraction limited spot size of the particle using

$$d_\tau \approx \left(M_O^2 d_p^2 + d_s^2 \right)^{1/2} \quad (2.7)$$

where d_p is the mean particle diameter and d_s is the diffraction limited spot size given by

$$d_s \approx 2.44 (1 + M_O) f^{\#} \lambda. \quad (2.8)$$

The tracer particles used are too small to optically resolve and light scattered from them appear as point sources. The image of a point object is always broadened by diffraction. The d_s terms represents this broadening and in many cases, $d_s \gg M_O d_p$.

Peak locking is a bias error where particle displacements trend towards integer values. A

common source of peak locking is having particles images smaller than one pixel. This can be mitigated by having particles occupy at least 2 adjacent pixels, $d_\tau / d_r > 2$ where d_r is the pixel pitch of the CCD sensor. Adrian [5] claims that random error is proportional to d_τ / d_r , but more recent work by Timmins [8] show that random error does not necessarily increase with particle image size. Timmins also showed that bias error is minimized when $d_\tau \approx 2.5$.

It has been shown by Keene and Adrian [7] that more than 8 particles inside of an IW results in a better than 95% probability of producing a valid vector. Particle seeding is often specified in units of particles per pixel (PPP). This metric can be determined from raw particles image by the DaVis software. Multiplying PPP by the number of pixels in an IW, e.g. $\text{PPP} \times \text{IW}^2$, estimates how many particles will be inside an average IW. It is often not possible to obtain a particle seeding density with sufficient PPP to have 8 particles per IW.

Limiting particle displacement allows a sufficient number of particles to appear inside the same IW for sequential images and results in a stronger correlation peak. However, higher displacements result in higher dynamic velocity range. The work of Wilson and Smith [9] demonstrates that a particle displacement of 10 pixels provides sufficient dynamic range to accurately resolve statistical quantities such as Reynolds stress. The initial IW window size is chosen to be at least 4 times larger than the displacement and rounded up to the nearest power of 2. This provides sufficient particles in both images for the initial pass and retains the speed increase of the FFT. Limiting particle movement in the fastest part of the flow means that particles near boundaries and shear layers will have less displacement between images. This results in lower dynamic velocity range and higher relative uncertainty.

2.3.2 Processing Algorithm

The 4th annual PIV challenge, in which multiple research teams analyzed the same data found that the largest uncertainties are introduced by the processing parameters selected by the user [10]. As many of the varied processing parameters affect different aspects of the PIV algorithm, this section describes the PIV algorithm specific to Davis 8.3.1 and its options. Exact implementation details for each processing step are covered in the DaVis Manuals [11, 12]. A typical PIV algorithm

can be broken into three steps: pre-processing of the images, vector calculation, and post-processing of the vectors.

Pre-Processing

Pre-processing attempts to increase the signal to noise ratio (SNR) of particle images by removing contributions to pixel intensity from anything that is not a particle. The three pre-processing methods to be investigated for the proposed thesis are sliding background subtraction, particle intensity normalization, and a Butterworth filter.

Subtraction of a sliding background acts as a spatial high pass filter to remove large intensity fluctuations in the background while the small intensity fluctuations of the particle signal pass through.

To remove background noise that vary in intensity over time, such as laser reflections, a Butterworth filter is useful. As reflections typically move slower than particles this allows a high-pass filter to remove the slow moving, lower frequencies of laser light reflections. Butterworth filter is chosen as a temporal high-pass filter for its flatness in its passband [13].

Particle intensity normalization applies a local particle intensity correction. It uses the minimum and maximum intensity values on a window defined by the scale length to normalize the intensity values of particle images. This homogenizes particle intensities and allows for dimmer particles to contribute to the correlation peak.

Vector Calculation

Vector calculation is the most important process where the instantaneous vector field is determined. This process has a large number of options and can be accomplished using 3 different methods: CPU, GPU, and PIV+PTV. The CPU method uses the CPU to calculate the correlation peak by exploiting properties of the convolution theorem and the Fast Fourier Transform. Implementation details are covered by Adrian [5]. This method is efficient and also tracks multiple correlation peaks. Secondary peaks can be used to determine if the primary peak produces an invalid vector.

Included as a subset of CPU processing is the Sum of Correlation Method. Sum of Correlation is an ensemble averaging method normally applied to micro PIV that only produces an average

vector field. The method is potentially useful for the proposed thesis as only the mean flow is required to determine volume-flow-rate. Sum of Correlation works by summing correlation planes from all image pairs before determining vector displacement. The average vector field is computed from an average of the correlation plane rather than using vectors from instantaneous vector fields to form an average. This provides a high-quality vector field of the mean flow from sub-par particles image at the expense of statistics. A multi-pass algorithm works repeatedly through the whole set. The vector calculation time is very low but high rates of data transfer from the hard disk cause this method to be slower than regular CPU processing.

GPU processing uses a direct correlation, which is computationally slow on a CPU, but can take advantage of the massive parallel throughput of a video card (GPU). The method is several orders of magnitude faster than CPU processing. The benefit of tracking multiple correlation peaks is lost as GPU processing only identifies the most prominent peak. GPU processing requires that the maximum pixel displacement be known to ensure a large enough search area to capture the correlation peak.

PIV+PTV is a combination of PIV and Particle Tracking Velocimetry (PTV). PTV differs from PIV in that it identifies and tracks the displacement of individual particles. PIV images generally have too high of a particle density for PTV. In PIV+PTV, a displacement vector field is determined through PIV that is then further refined by detecting and tracking individual particles. This produces a sparse vector field with a vector pitch of 1 pixel. In addition to the regular PIV parameters, this algorithm also requires the particle image size, intensity threshold of a particle image, correlation window size and a maximum search range be specified.

All of the vector calculation algorithms share several common processing options: An iterative, multipass scheme with IW that vary by size, weighting, overlap, and number of passes. The accuracy, spatial resolution and dynamic range improvements of a multi-pass scheme are well established [5] and are not discussed here. Each pass produces an estimate of the vector field that is then used to deform the second PIV image of each pair. A perfectly known vector field with no through-plane motion should cause the first image to be a copy of the second image. Additional passes use the deformed images to produce vector fields that are used to correct the previous pass vector

field. In addition to the IW options discussed above, there are several multipass options as well as multipass post-processing, where spurious vectors are identified and removed before deforming the images. All of these options are common to all three methods: CPU, GPU, and PIV+PTV.

Post-Processing

The final step in a PIV algorithm is post-processing, where spurious vectors are identified and removed. The two methods to identify spurious vectors for this thesis are a median filter and Q-ratio. The median filter works by computing a median vector from a group of neighboring vectors and comparing the middle vector with this median vector \pm deviation of the neighboring vectors. This is done independently for each component of velocity and can be done iteratively.

The Q-ratio, which is separate from Q used to define volume-flow-rate, is a type of signal to noise criteria. It is the ratio of the two largest correlation peaks. Typical values range from 1.3 to 3.0.

2.4 Measuring Volume-Flow-Rate

Both 2C and Stereo PIV have unique complications in calculating volume-flow-rate.

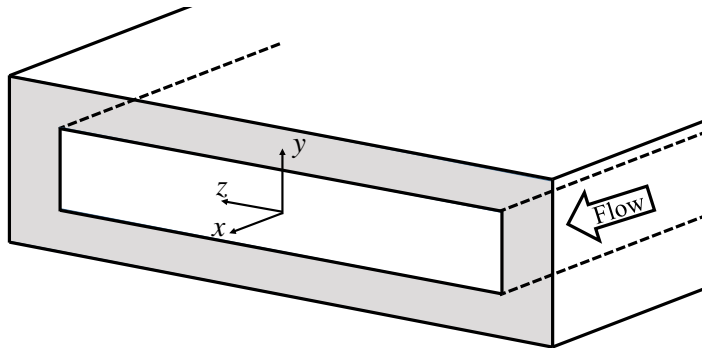


Fig. 2.2: Nozzle coordinate system.

2.4.1 2C PIV

Volume-flow-rate from 2C PIV is determined by acquiring data at several locations in the z dimension of the nozzle as shown in Fig. 2.3. The resulting velocity profiles are then averaged in

space. Data obtained during shakedown will be used to choose measurement plane locations.

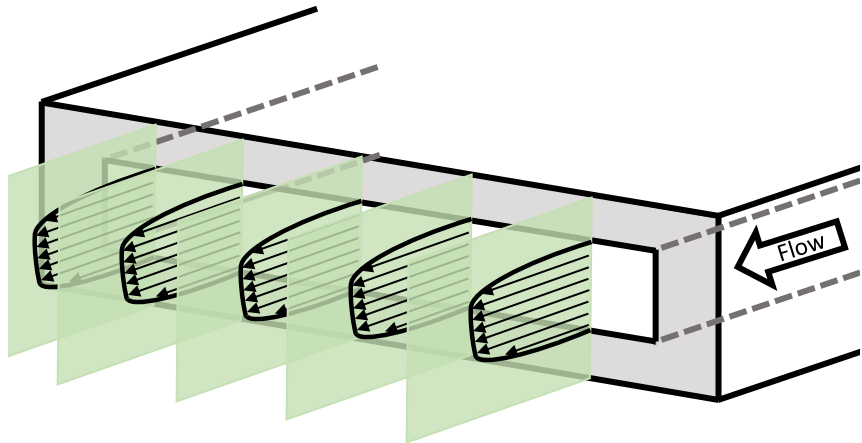


Fig. 2.3: 2C PIV setup for measuring volume-flow-rate. Measurement locations for 2C PIV are shown as a velocity profile illuminated by a laser sheet. Several example locations are shown.

2.4.2 Stereo PIV

For Stereo PIV, fluid flow can be measured across the entire exit of the nozzle. Because the laser sheet has finite thickness, fluid close to the nozzle exit is entrained and included in the measurement, leading to a potential volume-flow-rate error. This can be seen in Fig. 2.4 where the measurement volume is defined by a Gaussian laser sheet. Fluid entrainment occurs at the exit plane of the nozzle which is inside of the measurement volume.

To calculate the three components of velocity, images from each camera are mapped (de-warped) onto the measurement plane. Calibration images from each camera of a special target plate are used to create the dewarping map. Ideally, particles from both images will be mapped to the same location but any errors in the mapping procedure will cause a mismatch between the two images. A common error occurs when the calibration plane is not aligned with the measurement plane. Fig. 2.5 shows a shift of the laser sheet, or measurement plane, towards the cameras. When the images are dewarped to the calibration plane this creates a disparity in the particle location

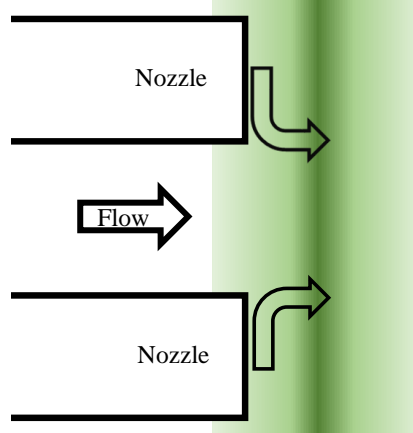


Fig. 2.4: Side view of a planar nozzle for stereo PIV measurements. The Gaussian nature of the laser sheet covering the exit plane limits how close it can be placed. Arrow outside of the nozzle show fluid being entrained inside of the measurement plane. This increases the volume-flow-rate of the measured flow.

between the two cameras [14].

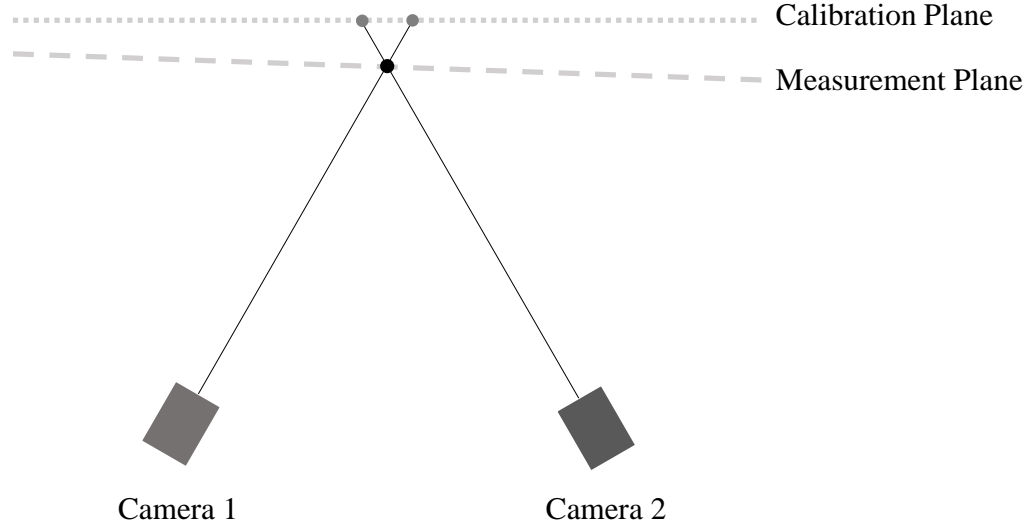


Fig. 2.5: A common stereo PIV calibration error occurs when the calibration plane and the measurement plane do not perfectly align. A shift of the calibration plane towards the cameras will cause the same particle to appear in two different locations.

To correct for misalignment between the calibration and measurement planes, a second calibration step is used. This second step is called self-calibration and described by Wienke [15]. A

disparity vector map is determined by performing a correlation between two images taken at the same time. Because both images are taken at the same time, any particle disparity between the two images is a misalignment between the measurement plane and calibration plane (assuming the cameras have remained unmoved).

Performing an accurate self-calibration has been shown to be vital for high-quality stereo PIV data [10]. Stereo PIV measurements inside of a pipe performed by van Doorne and Westerweel showed that small misalignments between the laser sheet (measurement volume) and calibration plane can cause large velocity errors, especially in regions of high shear [1].

2.4.3 Calculating Volume-Flow-Rate

The output of PIV is a regularly spaced vector field. For Stereo PIV, equation 2.2 can be used to calculate Q where Δy and Δz are the vector pitch in their respective dimension.

For 2C PIV, there is a large amount of velocity data in the y dimension but relatively sparse velocity data in the z dimension as shown in Fig 2.3. Previous work shows the velocity profile in the z dimension largely consists of a flat core section and sharp shear layers [3, 16–18]. It is therefore reasonable to interpolate across the z dimension between measurement planes.

2.4.4 Volume-Flow-Rate Uncertainty

Uncertainty analysis should consider both random and bias sources.

Random uncertainty is unlikely to have a significant effect on the total volume-flow-rate uncertainty since all data are averaged in time and then in space. A major objective of this work is to assess the effect of PIV processing parameters on volume-flow-rate measurements. While the impact of processing parameters on random uncertainty is discussed below, the uncertainty of the volume volume-flow-rate will be assumed to be a function of bias uncertainty only.

PIV measurement error has been extensively investigated using theoretical modeling [19], Monte Carlo simulations [20], and experiments [21]. Bias, or systematic errors, in PIV are typically caused by calibration errors and inadequacy of the interrogation algorithm by pixel locking [5]. Random errors have multiple sources that include: camera noise, background illumination, out-of-plane particle movement, shear, and others.

The uncertainty analysis shown here is restricted to a single measurement plane with the understanding that uncertainties for each measurement plane can be determined individually and combined for the total uncertainty of Q . We will therefore drop the j index from Eq. 2.2 which is used as the data reduction equation. Bias uncertainty can be expressed using the Taylor series method of propagation of uncertainties as

$$b_Q^2 = \left(\frac{\partial Q}{\partial \Delta y} b_{\Delta y} \right)^2 + \left(\frac{\partial Q}{\partial \Delta z} b_{\Delta z} \right)^2 + \left(\frac{\partial Q}{\partial \bar{u}_1} b_{\bar{u}_1} \right)^2 + \left(\frac{\partial Q}{\partial \bar{u}_2} b_{\bar{u}_2} \right)^2 + \cdots + \left(\frac{\partial Q}{\partial \bar{u}_{N_y}} b_{\bar{u}_{N_y}} \right)^2. \quad (2.9)$$

Individual instantaneous velocity vectors are computed using

$$u_i = \frac{sf \Delta x_i}{\Delta t} \quad (2.10)$$

where Δx and Δt are particle displacement and time between image pairs, respectively, and are assumed to have no bias leaving bias uncertainty a function of the scaling factor, sf . This assumption relies on particle image diameters (d_τ) of sufficient size. Care was taken to ensure optimal particle image diameters during data acquisition. These instantaneous velocities are time averaged to compute \bar{u}_i . Since Δz is a constant for each measurement plane and Δy is a constant for all measurement planes in the same data set, all velocity vectors share the same bias uncertainty. Evaluating the partial derivatives, Eq. 2.9 can be rewritten

$$b_Q^2 = (\Delta z \sum \bar{u}_i)^2 b_{\Delta y}^2 + (\Delta y \sum \bar{u}_i)^2 b_{\Delta z}^2 + N_y (\Delta y \Delta z)^2 b_{\bar{u}_i}^2. \quad (2.11)$$

Uncertainty in Δy is only a function of scaling factor. Scaling was determined by focusing on the outside edge of nozzle, $z = W/2$. The glass composing the side of the nozzle is used as a reference plane with known dimensions.

Instantaneous uncertainty calculated from DaVis does not account for uncertainty in the scaling factor. The scaling factor is $sf = X_n X_p$ where X_n is the nominal dimension (in mm) and X_p is the dimension on the sensor of the camera (in pixels). Using the Taylor series method of uncertainty

propagation, the uncertainty of the scaling factor is

$$\left(\frac{U_{sf}}{sf}\right)^2 = \left(\frac{U_{X_n}}{X_n}\right)^2 + \left(\frac{U_{X_p}}{X_p}\right)^2. \quad (2.12)$$

Sources of uncertainty for the nominal measurement include the calipers used to measure the nominal dimensions of the nozzle and error induced by a changing Field Of View (FOV) due to the traverse spatial resolution. Uncertainty of the calipers is the largest uncertainty value on the calipers calibration documentation. This value is equal to the smallest tick. As discussed earlier, an error may exist between the desired camera position and the actual camera position causing a small change in the FOV. The uncertainty from this error on the FOV is sub-micron. Following the “rule-of-quarters” [22] that any elemental uncertainty one-fourth or smaller of another uncertainty can be ignored, we ignore changes in the FOV resulting from traverse resolution as uncertainty.

There are two sources of uncertainty for X_p . Half of the spatial resolution of the camera (0.5 pixels) and human judgment. Less than perfect lighting require some level of interpretation to identify the edges of the jet exit. The edges of the exit were clear within 2 pixels. Evaluating Eq. 2.12 gives a relative uncertainty to the scaling factor of 0.28%.

Instantaneous random uncertainty stemming from the vector computation is calculated by the DaVis software. Random uncertainty of the mean is also computed by DaVis:

$$s_{\bar{u}_i} = \frac{s_{u_i}}{\sqrt{n}}. \quad (2.13)$$

Random uncertainty is unlikely to have a significant effect on the total volume-flow-rate uncertainty as all data will be averaged in time and then integrated in space.

Random uncertainty will be discussed since it is relevant to the study of PIV processing parameters. The quality of various processing schemes will be assessed, in part, based on random uncertainty. It was shown in [21] that for Gaussian error distributions, the variance of the error is equal to the variance of the random uncertainty. We therefor use the variance of the random instantaneous uncertainty to assess the efficacy of processing parameters.

Random instantaneous uncertainty is determined using correlation statistics method as presented by Wieneke [23]. It is a generic uncertainty estimation method that can be applied as a post processing step and only requires the particle images and the vector field calculated from them. This makes the method independent of how the vector field was calculated, whether it be CPU, GPU, or PIV+PTV.

Similar to the particle disparity method presented by Sciacchitano [24], correlation statistics uses the original first image and a second image is upsampled and distorted based on the previous-pass velocity field. While the particle disparity method uses individual particle disparity, the correlation statistics method uses the standard deviation of the pixel-wise contribution of intensity differences in the shape of the correlation. This statistical quantity is related to the random uncertainty of the displacement vectors.

The correlation statistics method has been shown to be accurate on synthetic data [23] and experimental data [21] with a few caveats. While it shows good agreement with random error distributions, it underestimates error for 16×16 IW. Additionally it is not able to estimate bias error, e.g. peak-locking. We note that, as described above, peak locking errors have been eliminated in the present study by ensuring ideal particle image diameter.

2.4.5 Metrics

The end goal of this project is to determine how to accurately measure the volume flow through a planar jet. We use several metrics to assess the performance of the data acquisition and comparison to a “ground truth” value from a high-accuracy flow meter is used to determine the volume-flow-rate error. This metric is not sufficient and may, in some circumstances, provide misleading information. A positive error in data acquisition causing flowrates to appear high could be offset by a negative error in a certain processing option. To mitigate issues like these, the random uncertainty of the time-mean Eq. 2.13 introduced as a second metric. We note that s_u is a function both of real velocity fluctuations and random measurement uncertainty [25]. Therefore, an increase in this value leads to an increase in the volume-flow-rate uncertainty, but this could be due to a better-resolved measurement and the associate increased random uncertainty of the mean.

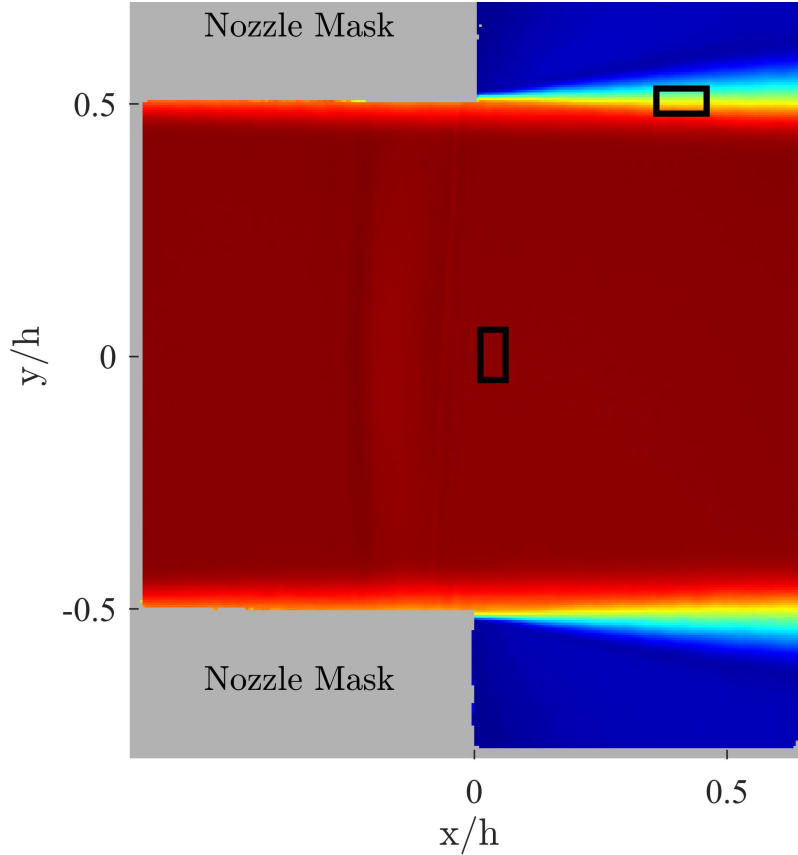


Fig. 2.6: Mean velocity field for Reynolds number = 100,000 at the $z = 0.00$ location. Boxed locations identify where uncertainty was taken to represent the core and shear flow regions.

Some processing steps that are expected to lead to improved accuracy and thus a decrease in the instantaneous random uncertainty are found to result in an increase in the random uncertainty of the mean. These results are investigated further to determine if the increase in uncertainty of the mean is caused by better resolved flow measurements or increases in the random uncertainty of instantaneous measurements. We note that, as discussed in [25], Reynolds normal stress, which is equal to the variance of velocity, is impacted by random uncertainty. Assuming Gaussian error distributions,

$$\overline{u'u'}_{meas} = \overline{u'u'}_{true} + s_{U_u}^2 \quad (2.14)$$

where $\overline{u'u'}$ is the Reynolds normal stress and U_u is the instantaneous velocity uncertainty. Both random uncertainty of the mean and random instantaneous uncertainty are examined individually by focusing on a region in the shear layer of the jet and a region in the core. Locations where the

uncertainty is reported are shown in boxes in Fig. 2.6. Random uncertainty of the mean is spatially averaged over the marked locations. Random instantaneous uncertainty is assessed by computing the standard deviation of the instantaneous uncertainty and then averaging in space for the two regions. Instantaneous uncertainties are determined using the Correlations Statistics method [23].

Calculation time is used as a third metric. The calculation time is only available for processing options during the vector calculation portion of the PIV algorithm.

CHAPTER 3

Equipment

3.1 Test Facility

Fig. 3.1 shows the test facility used to acquire data. It is an unpressurized, closed circuit flow loop in a vertical configuration and holds 72 gallons of water. It has a 6" × 6" × 36" glass section coated to be anti-reflective to light at 532 nm. Flow straighteners and a contraction nozzle are used to ensure a near "Top Hat" profile at the jet exit.

It has a modular design allowing for different nozzles. Flow is driven by a centrifugal pump designed to deliver 370 GPM against a pressure of 11'6" of water and coupled to a 3HP TEFC, 1800 RPM motor using 208-230V AC/3Φ/60Hz/5 amp service and controlled by a variable frequency inverter. Schematic drawings of the facility are shown in Fig. 3.2 and Fig. 3.3.



Fig. 3.1: Test facility used to acquire data. Flow circulates in a clock-wise direction.

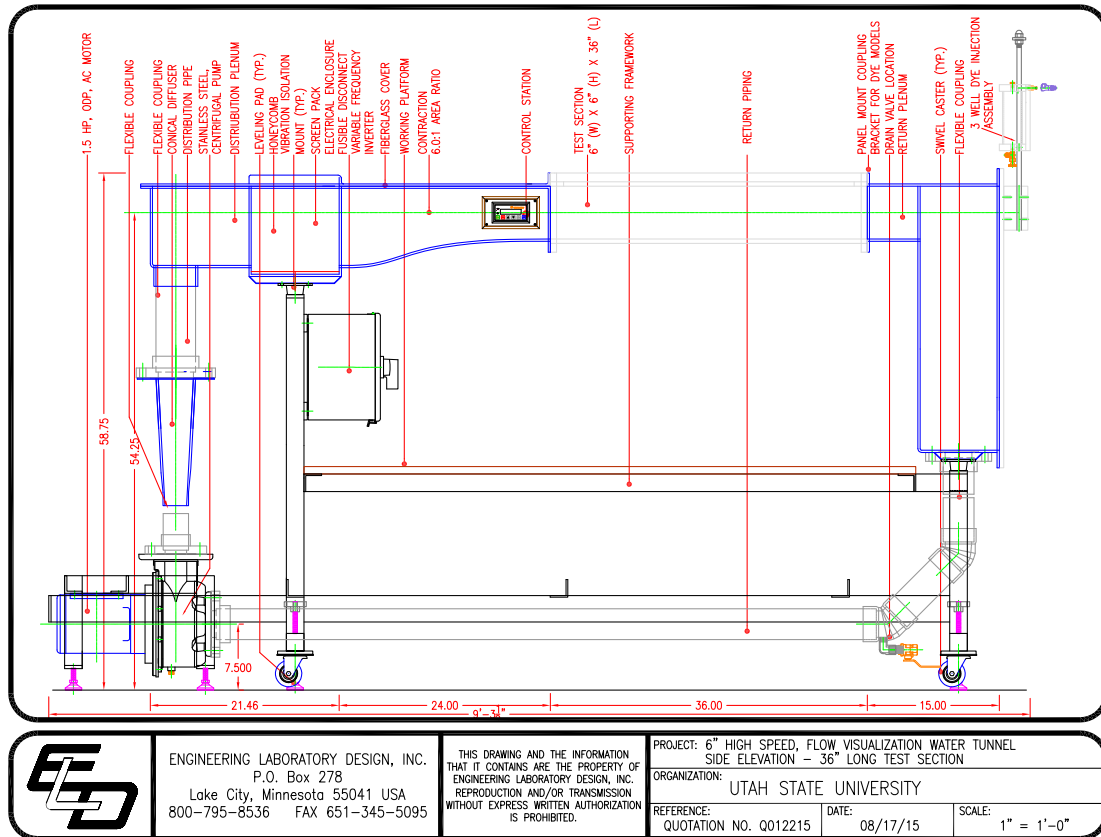


Fig. 3.2: Side-view schematic of test facility used to acquire data. Flow circulates in a clock-wise direction.

3.2 Flow Meter

The volumetric flowmeter acts as the benchmark for our integral scale measurements. In other words, if the PIV measurements match the flow meter, we may claim that they are as accurate as the uncertainty of the flow meter. The flowmeter is a *Rosemount Inc.* Model 8705 Magnetic Flowmeter Flowtube with an accuracy of $\pm 0.5\%$ of reading for flows greater than 0.011 m/s. The analog output ranges from 4-20 mA scaled linearly over a range of 105 GPM. Current is passed through a high precision resistor where voltage is measured with a 16-bit data acquisition system which is itself scaled over a 10-volt range. This gives sufficient resolution to detect a 0.004% of full-scale reading change. The flowmeter requires that the water have a minimum conductivity of 5 $\mu\text{S}/\text{cm}$. Conductivity was measured to be 175 $\mu\text{S}/\text{cm}$ using a HM Digital Water Tester model AP-2, which has a resolution of 1 μS and an accuracy of $\pm 2\%$ of reading. The water tester was calibrated against

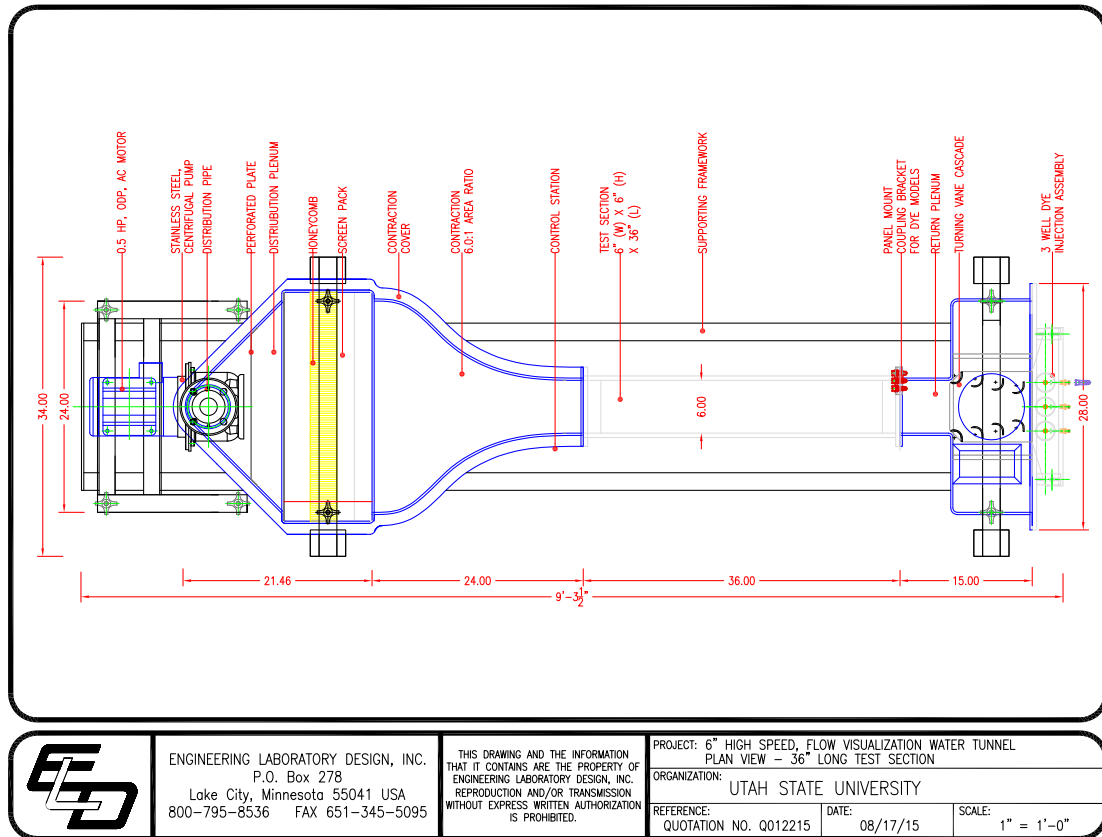


Fig. 3.3: Top-view schematic of test facility used to acquire data. Flow is driven from left to right.

a solution of 342 ppm NaCl.

As delivered, power to the flowmeter was routed through same electrical box that contains the pump inverter. This introduced a large amount of noise to the analog signal. A separate power route was established using isolated connectors and shielded cables to bypass the electrical box powering the water tunnel. Establishing an isolated power supply reduced the noise by an order of magnitude. The remaining noise is filtered digitally using a median filter with a rank equivalent to 50 ms during data acquisition.

3.3 Nozzle

The nozzle used for this study is a high aspect ratio, planar nozzle. Fig. 3.4 shows the rectangular nozzle used to acquire data. The exit of the nozzle is glass coated to be anti-reflective to light at 532 nm. Fig. 3.5 and Fig. 3.6 show schematic views of the nozzle installed in the test facility. Fig.

3.7 shows the as built measurements of the nozzle exit. Measurements were made using *Mitutoyo* model D8"HN dial calipers with graduation markings of 0.001". The nozzle has a mean height of $0.4313" \pm 0.001"$ and a width of $4.331" \pm 0.001"$, giving an aspect ratio of 10.04 ± 0.02 .

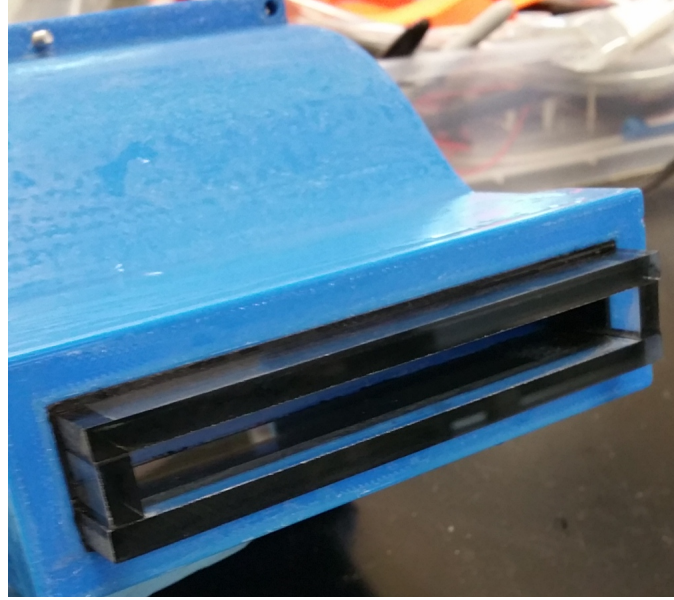


Fig. 3.4: High aspect ratio, rectangular nozzle used to acquire data.

The Reynolds number is based on the hydraulic diameter of the nozzle. Hydraulic diameter is

$$D_h = \frac{2HW}{H + W} \quad (3.1)$$

where H is the height, or small dimension of the nozzle and W is the span, or long dimension of the nozzle.

3.4 Camera

Data were acquired using LaVision Image sCMOS cameras. Camera resolution is 2560×2160 pixels with a bit depth of 16 bits. Pixel size is $6.5 \mu\text{m} \times 6.5 \mu\text{m}$ and total sensor size is $16.6 \text{ mm} \times 14.0 \text{ mm}$. Frame rate is 50 fps at full resolution. The minimum interframing time is 120 ns.

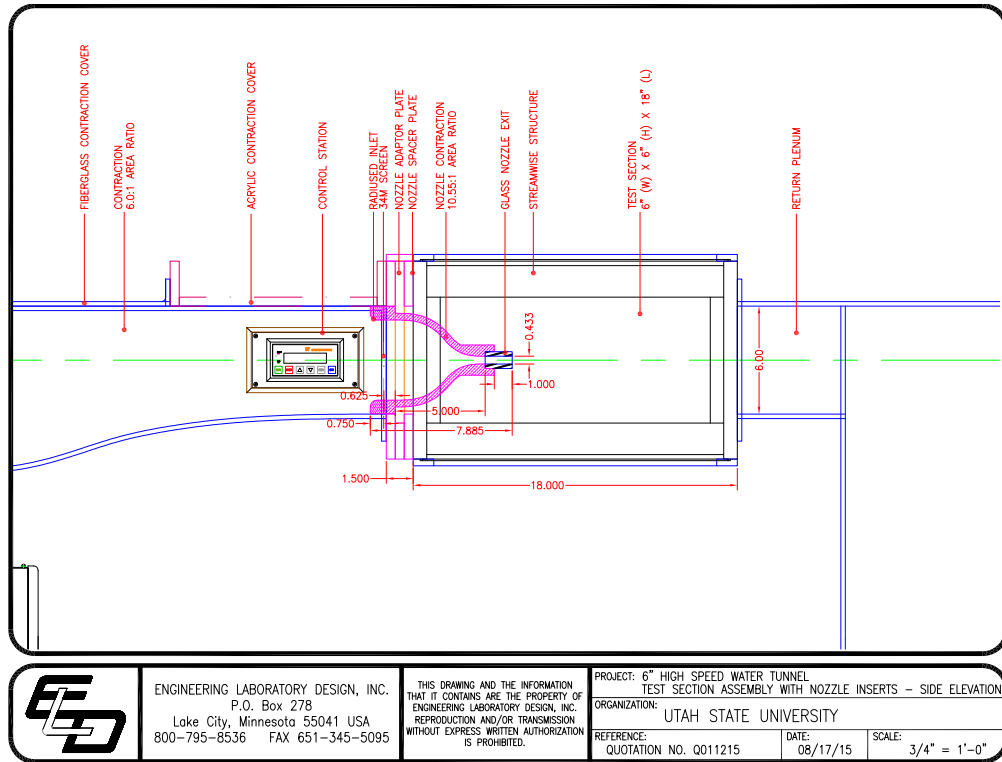


Fig. 3.5: Side view schematic of nozzle used to acquire data. Flow is driven from left to right.

3.5 Optics

Two camera types of lens were used for this study. A 105 mm f/2.8D Macro lens and a 28 mm f/2.8 wide-angle lens. The 28 mm lens was only used to collect 2C PIV data in the x - z plane as part of the facility shake down. All other data were acquired using 105 mm optics.

3.6 Laser

The laser is a Quantel EverGreen model 25100. It is a frequency doubled Nd:YAG laser that produces light at 532 nm. It can produce 100 mJ/pulse at 25 Hz. The laser passed through a spherical and then cylindrical optics to produce a laser sheet. Laser sheet thickness was measured by burning into photo-sensitive paper. The paper used was ZAP-IT® Laser Alignment Paper from Kentek®. The minimum laser sheet thickness is determined to be 0.94 mm.

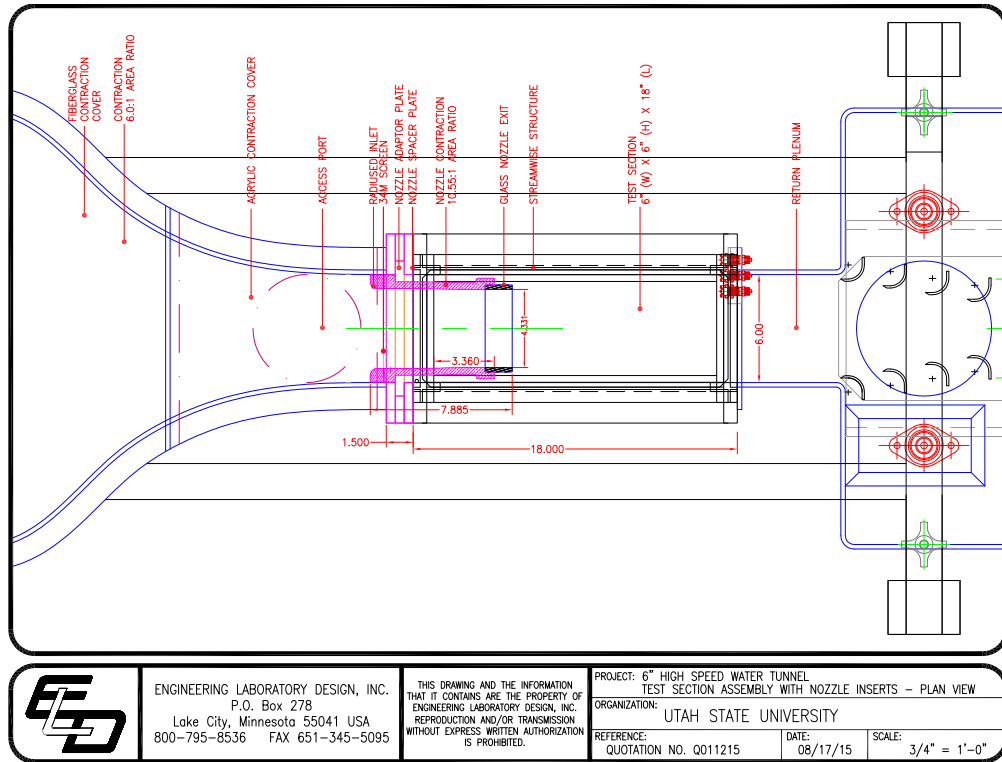


Fig. 3.6: Top down view schematic of nozzle used to acquire data. Flow is driven from left to right.

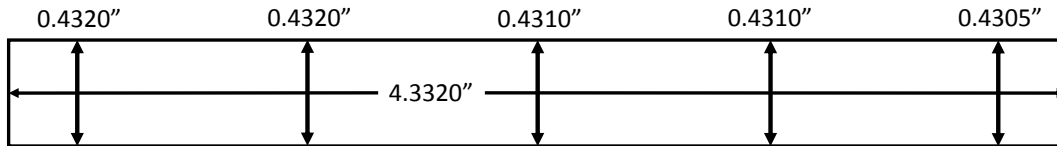


Fig. 3.7: As built, internal dimensions of the nozzle at the exit plane.

3.7 Calibration Plate for Stereo PIV

Fig. 3.8 shows the calibration plate used for stereo PIV. The calibration plate serves as a two-level reference plane as discussed in Section 2.4.2 and is mounted 2.1 mm behind the exit of the nozzle. The calibration algorithm in DaVis was unable to detect the reference marks both above and below the nozzle at the same time. Using reference marks on both sides of the nozzle would allow interpolation of the calibration over the exit of the nozzle. Using only one side of the calibration plate would require the extrapolation of the calibration for the nozzle exit.

Both cameras were lowered such that the calibration plate occupied the lower 2/3 of their FOV. Calibration was performed with only the FOV occupied by the calibration plate considered

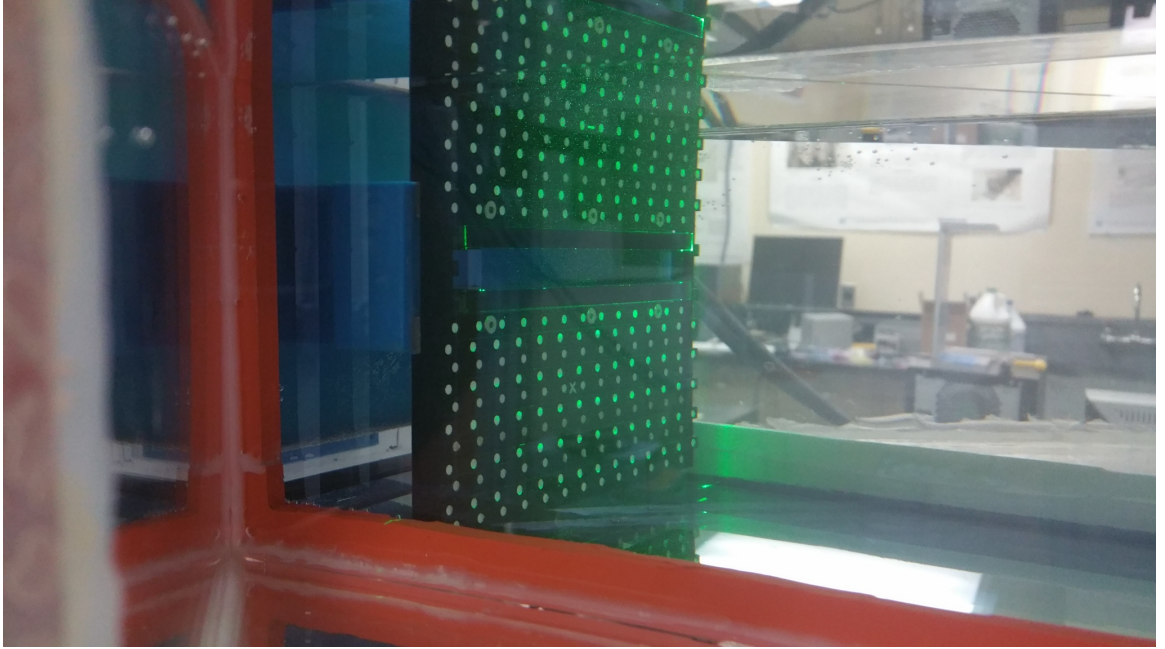


Fig. 3.8: Calibration plate used for stereo PIV measurements.

to be calibrated. After calibration, the cameras were raised until the nozzle occupied the calibrated portion of their FOV. Both cameras were attached to an optical rail that was itself mounted to a Newport High Load Lab Jack, allowing both cameras to be moved at once.

Self calibration was then used to shift the calibration plate to the measurement plane, defined by the laser sheet, at the exit of the nozzle.

3.8 Stereo PIV Setup

Cameras were arranged on either side of the test-section at an angle of 45° . From this angle, changes in the index of refraction cause a large amount of distortion of the nozzle exit. Snell's law is

$$n_1 \sin \theta_1 = n_2 \sin \theta_2 \quad (3.2)$$

and describes the relationship between the relationship between the angles of incidence and refraction for light passing through a boundary. The n_1 and n_2 terms are the index of refraction values for each material and are a fixed property. To reduce the amount of distortion a prism made from Plexiglas is mounted to the test section at the same angle as the cameras and filled with water. This

allows the air-water boundary, with the largest differences in their index of refraction's to occur at a minimal angle.

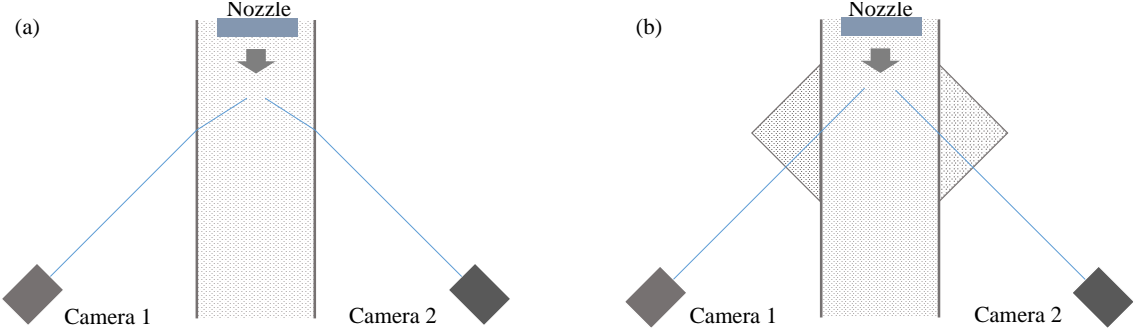


Fig. 3.9: Top down schematic of the facility. Subfigure (a) shows how large changes in the index of refraction at the air-water boundary cause optical distortion. Subfigure (b) shows how Plexiglas prisms mounted to the facility reduce the angle of incidence at the air-water boundary. Shaded areas represent locations filled with water.

Images taken at the same location, with (Fig. 3.10) and without a prism (Fig. 3.11) shows this effect.

3.9 Facility Operation

3.9.1 Flow Control

Volume-flow-rate is controlled by a variable frequency inverter with a range of 0.5-60 Hz in increments of 0.1 Hz. This produces a mean exit velocity through the nozzle of 0.09 m/s to 13.03 m/s in increments of 0.2 m/s. Reynolds number is determined as

$$Re = \frac{\bar{u}D_h}{\nu}. \quad (3.3)$$

The facility is capable of Reynolds numbers from 2000 to 260,000 in increments of ≈ 433 .

The viscosity of water has a strong dependence on temperature as shown in Fig. 3.12. A thermocouple was inserted into the return plenum of the water tunnel and tracked temperature changes at flows representing $Re = 10,000$ and $100,000$. At $Re = 10,000$, the temperature rose $0.11^\circ \text{C}/\text{hour}$

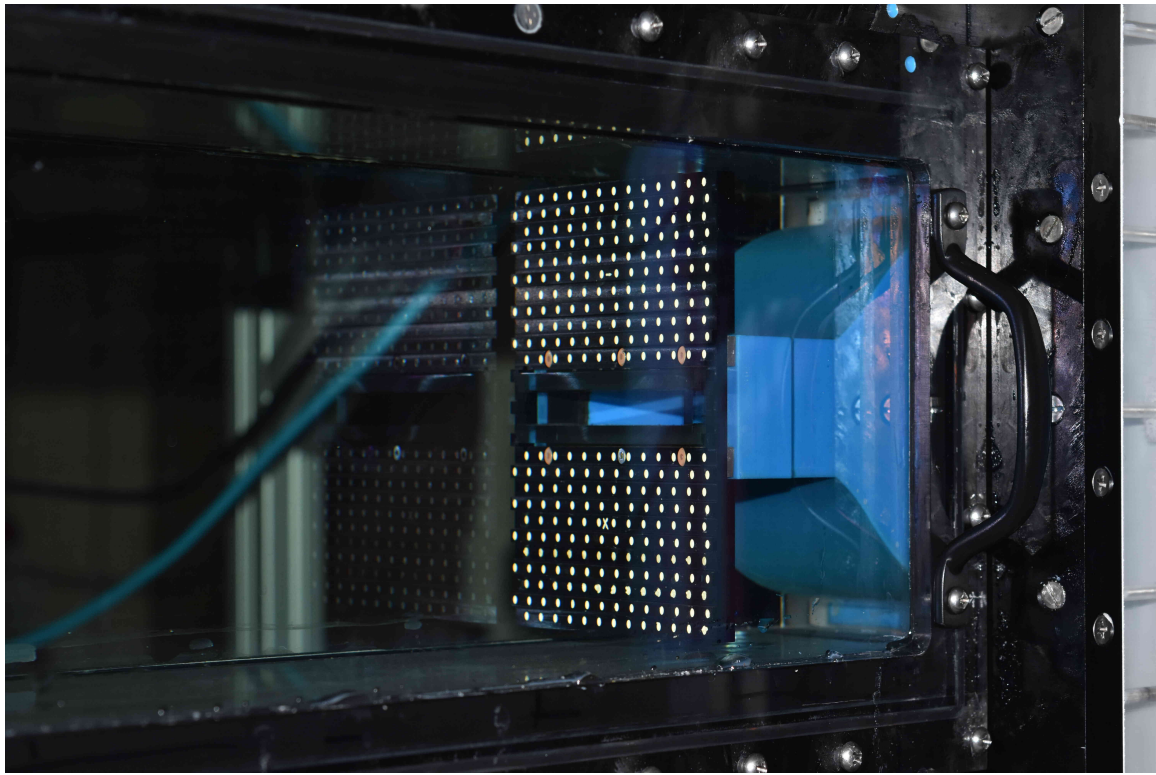


Fig. 3.10: View of the calibration plate without a water filled prism to correct for index of refraction changes.

and at $Re = 100,000$ rose $0.31^\circ \text{C}/\text{hour}$. At the higher Re , this temperature change corresponds to a power input of 91 Watts. The temperature rise means that viscosity changes roughly 0.2% and 0.7% each hour which affects the Reynolds number of the flow.

3.9.2 Particle Seeding

Spherice[®] 110P8 hollow glass spheres are used as seed particles. They have a mean diameter of $11.7 \mu\text{m}$ and a density of $1.10 \pm 0.05 \text{ g/cc}$. Particle seeding density is estimated using DaVis and recorded in units of PPP. Fig. 3.13 and Fig. 3.14 show raw particle images for 2C and Stereo PIV.

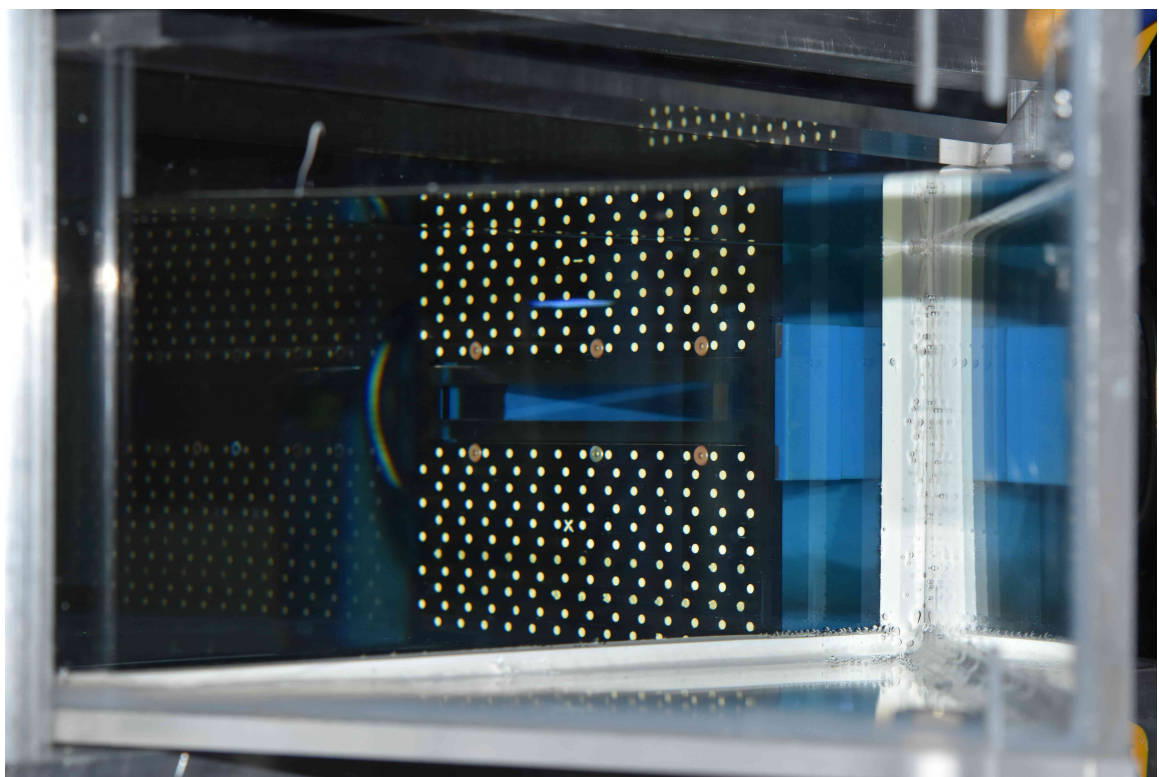


Fig. 3.11: View of the calibration plate with a water filled prism to correct for index of refraction changes.

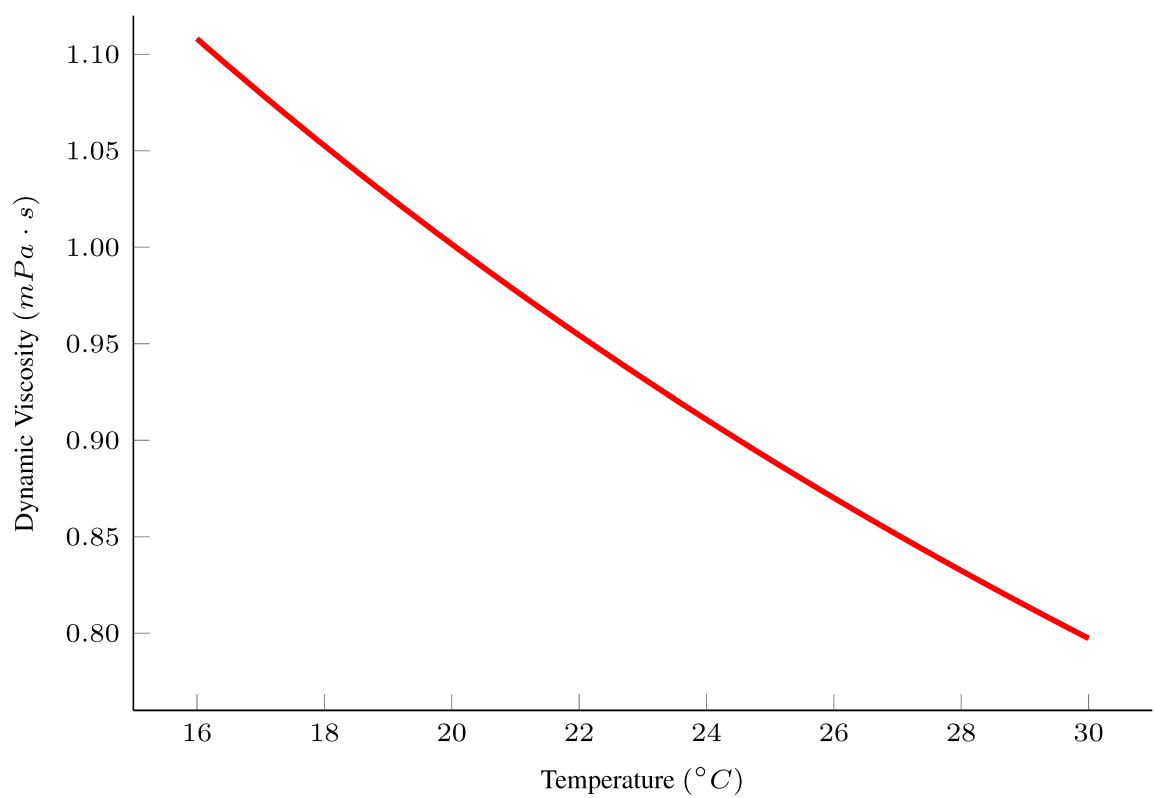


Fig. 3.12: Viscosity of water as a function of temperature.

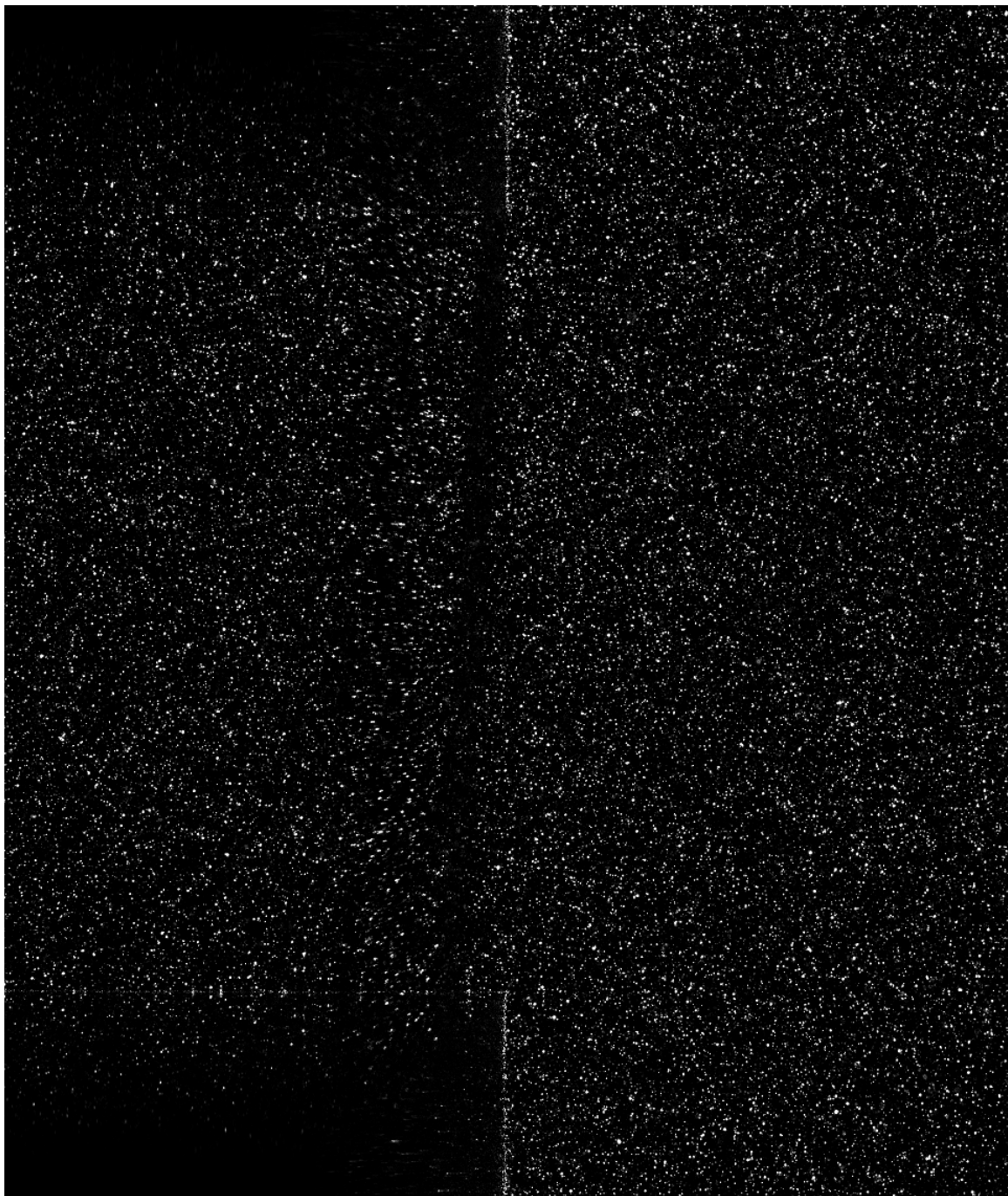


Fig. 3.13: Raw particle image for 2C PIV. The nozzle occupies the upper left and lower left portion of image. Particles that appear inside of the nozzle are caused by light reflecting off particles.

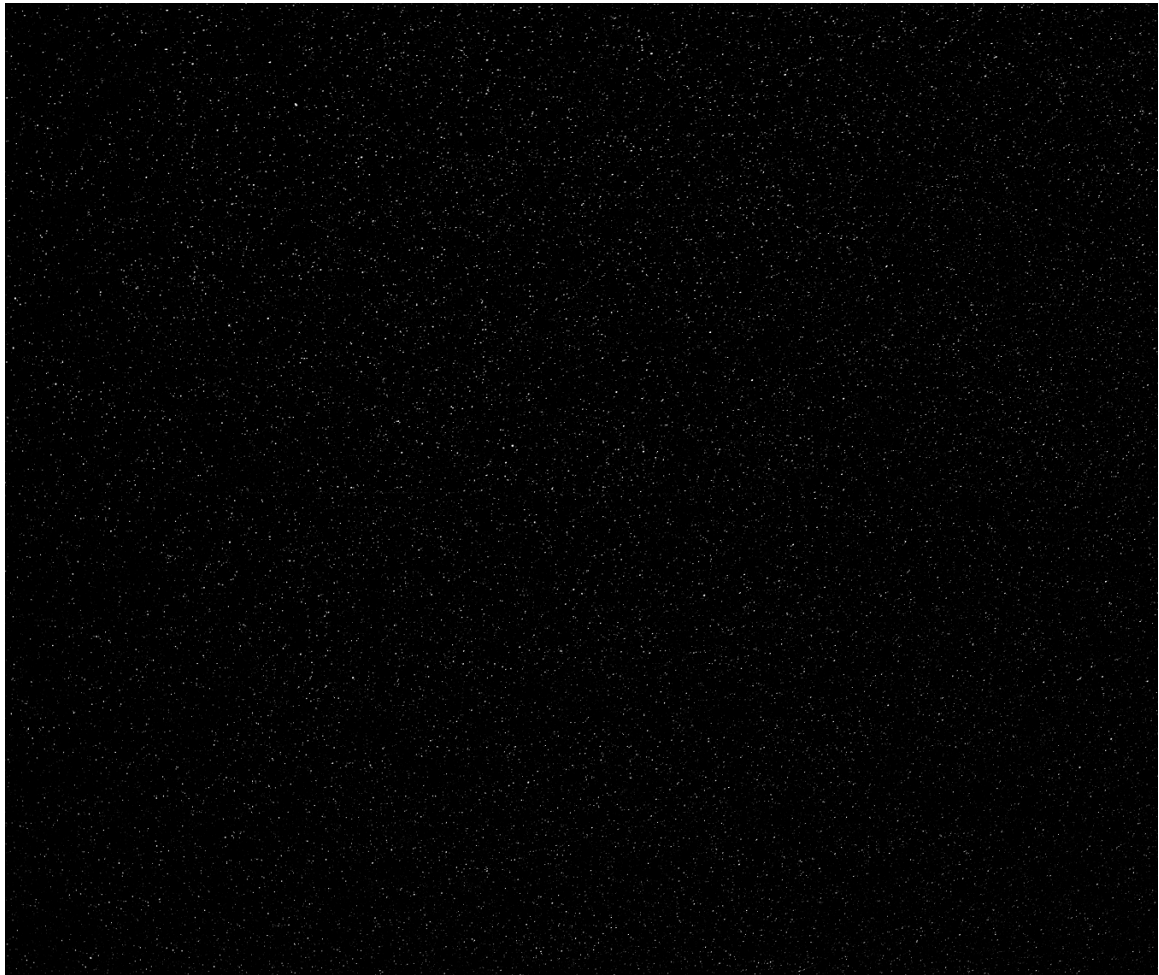


Fig. 3.14: Raw particle image for stereo PIV.

CHAPTER 4

Results

4.1 Facility Shakedown

Shakedown is performed as a series of tests to ensure the facility is operational, establish flow behavior, and identify potential problems. Two-component PIV was used to collect data in the x - y and x - z planes at Reynolds numbers of 10,000 and 100,000. Fig. 4.1 shows the coordinate system used and the orientation of the nozzle and laser sheet. Data were acquired at five locations in the x - z plane and 7 locations in the x - y plane. Table 4.1 shows these locations.

Several problems were identified during shakedown. Some of these problems are unique to this particular facility while others appear to be common issues for water tunnels. However, no warning for any of these issues was found in the literature. Identified problems and their solutions are included in this section.

Table 4.1: Data acquisition locations for facility shakedown.

y Location (mm)	x - y Planes		z Location (mm)	x - z Planes	
	-3.81	3.81		54.47	53.47
	-1.91			25.01	
	0.00			0.00	
	1.91			-30.01	
	3.81			-53.47	
				-54.47	

Seed particles in the tunnel were found to settle out and form a film on surfaces. During subsequent tunnel operations, this film can break into conglomerates much larger than individual particles. These conglomerates are large enough that they cannot pass through mesh screen at the jet inlet. In order to prevent this, it is necessary to filter out particles before shutting down the water tunnel. Running the water tunnel at $Re = 30,000$ while filtering for at least an hour appears to be

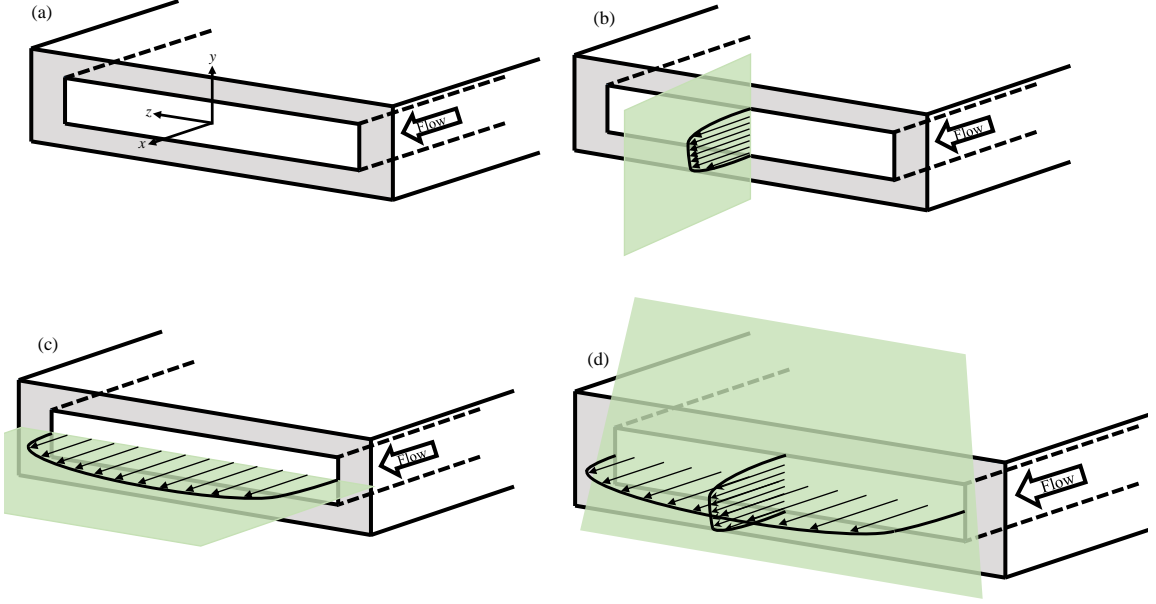


Fig. 4.1: Nozzle and laser sheet orientation. Subfigure (a) shows coordinate system centered at the exit plane. Subfigure (b) shows the orientation of the laser sheet for 2C PIV in the *x*-*y* plane. The laser sheet is shown as a green plane illuminating a velocity profile. Subfigure (c) shows the orientation for 2C PIV in the *x*-*z* plane. Subfigure (d) shows the orientation for Stereo PIV where velocity is measured over the exit plane of the nozzle.

sufficient to prevent film buildup.

Fig. 4.2 show velocity profiles for flow at $Re = 10,000$. All velocity profiles are taken at the exit plane of the nozzle ($x = 0$). Most of the profiles have a “top hat” profile. There is some deviation near the wall, especially the two outer profiles in the *x*-*z* plane. The dips in velocity are not localized events but extend downstream of the nozzle exit. This is evidence that these are flow artifacts and not measurement issues. The issue of particle conglomerates not passing through the mesh screen of the nozzle, as discussed previously, was not noticed until after this data set was acquired. It is likely that these streamwise vortices are caused by particle conglomerates on the mesh screen.

Several of the problems identified during shakedown were illuminated in the velocity profiles. Fig. 4.3 show velocity profiles for flow at $Re = 100,000$. The near wall data shows that the flow is turbulent and developing boundary layers are evident. As boundary layers develop, the flow profile deviates from a top hat. As the thickness of the boundary layer increases, conservation of

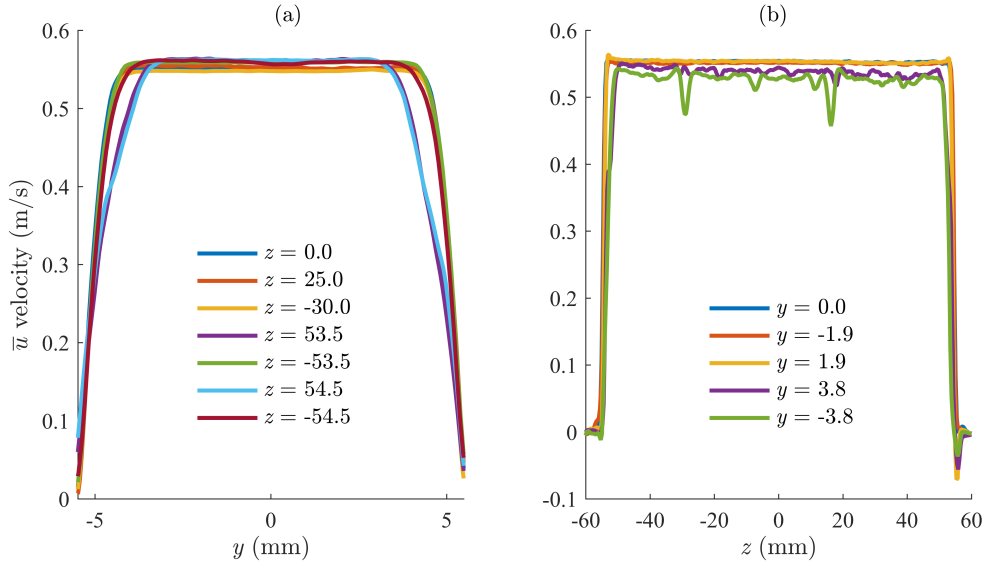


Fig. 4.2: Velocity profiles taken at the nozzle exit for $Re = 10,000$. Subfigure (a) shows average (\bar{u}) velocity profiles in the x - y plane. Subfigure (b) shows average (\bar{u}) velocity profiles in the x - z plane.

mass requires that some fluid move towards the faster moving flow near the center nozzle. This generates a small cross-stream velocity. This cross-stream velocity goes to zero once the flow is fully developed. There is not sufficient distance for the flow to fully develop in the length of the nozzle. Fig. 4.4 shows the cross-stream velocities for the developing flow for $Re = 100,000$ at $z = 53.7$ and $y = 3.81$. The profiles were similar for the other cases and locations.

It was found that flow was not fully turbulent until Reynolds numbers above 63,000 were reached.

Although these effects are prominent in the v and w profiles, these velocities are very small compared to the streamwise velocity. Depending on the orientation and location of the laser sheet, this has the potential to generate errors in 2C measurements due to magnification and perspective error. But, since these displacements are very small compared to the streamwise displacement they should have no appreciable impact.

Image scaling is required to determine the physical spacing between vectors and to convert particle displacement to a velocity measurement. Image scaling was initially performed by using the upstream of the exit plane and marking where the laser sheet illuminated the glass nozzle. This distance was assigned to the measured nozzle dimension. However, it was found that the full

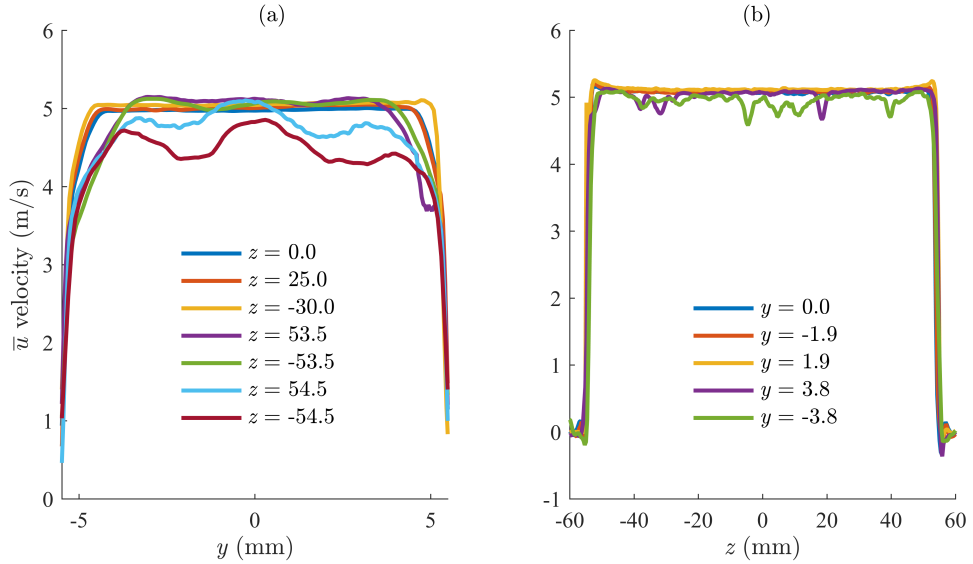


Fig. 4.3: Average velocity profiles (\bar{u}) taken at the nozzle exit for $Re = 100,000$. Subfigure (a) shows velocity profiles in the x - y plane. Subfigure (b) show velocity profiles in the x - z plane.

dimensions of the flow upstream of the exit plane could not be viewed due to a parallax in several of the x - y data sets. This was caused by the aperture of the camera being larger than height of the nozzle. In other words for measurement locations furthest away from the camera, the near parts of the nozzle blocked full view of the measurement plane upstream of the exit plane. At the exit plane and immediately downstream from the exit plane, seeding density was sufficient to determine where particle movement went to zero by eye. This location could reliably be determined within 3-4 pixels. The images were scaled on the shear layer dimension as determined by particles at the exit plane. This 3-4 pixel uncertainty is small compared to the size of the nozzle. For example, the x - y data set at $z = 53.47$ has a nozzle height of 1330 pixels, so 4 pixels represents about 0.3% of the total height. An uncertainty analysis following the guidelines of Coleman and Steele [22] show that uncertainty from scaling is small compared to other uncertainties and can be ignored. This method of finding the nozzle dimension was confirmed by processing the data set using a PIV+PTV processing algorithm, which returns the velocity at every pixel. The time-averaged vector field with a vector for each pixel shows the velocity going to zero at the nominal dimensions of the jet.

It is desirable to maintain a similar FOV for all measurement locations and to avoid issues caused by parallax. For the current measurement setup we have an optical path through several dif-

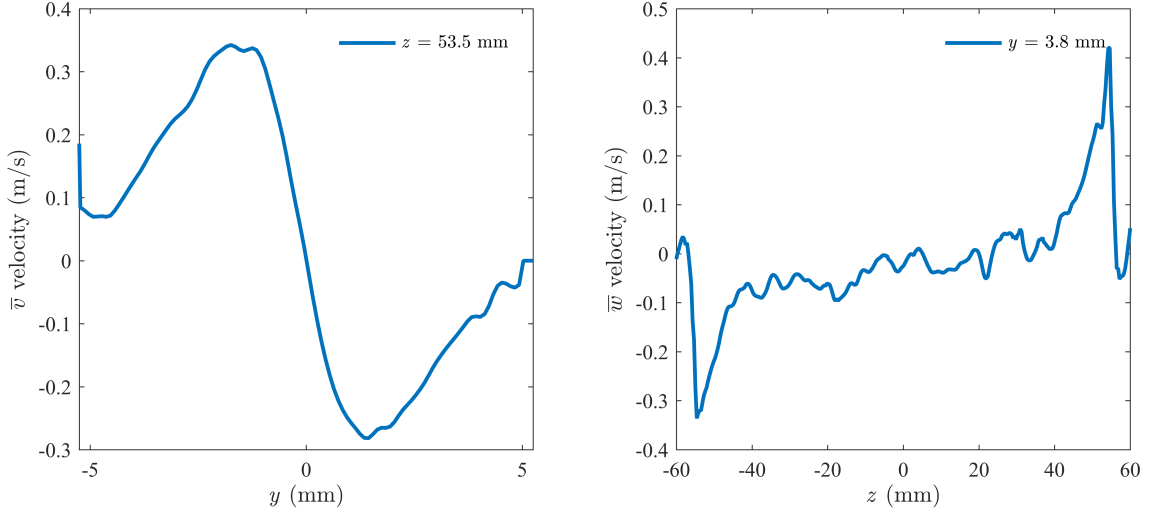


Fig. 4.4: Developing flow can be seen in cross stream velocity profiles near the edges of the nozzle in the x - y profile at $z = 53.5$ (a) and x - y profile at $y = 3.8$ (b) for flow at $Re = 100,000$.

ferent mediums: air, glass, and water. To maintain a similar FOV between measurement locations, changes in the index of refraction require the relative movement of camera and laser to be different from 1:1. Their relative movements are given by

$$\frac{dz_c}{dz_l} = \frac{\sin^{-1} \left(\frac{n_{air}}{n_{water}} \sin \theta \right)}{\tan \theta} \quad (4.1)$$

where the camera displacement, dz_c and the laser displacement, dz_l are based on the ratio of the index of refraction of each fluid and the viewing angle of the lens θ . The thickness and index of refraction of the test section glass are considered but the resultant terms cancel. The index of refraction of water can be determined using the equation presented by Thormahlen *et al.* [26] and uses 14 coefficients and accounts for wavelength, temperature, and density.

The exiting jet flow is unstable and appears to flap in the $\pm y$ directions. Both Reynolds number cases have the same Strouhal number of 0.0014 based on hydraulic diameter. This instability exists because the jet height is not sufficiently small compared the test section [27]. These events can only be seen in the x - y datasets and have a frequency of 0.05 Hz and 0.35 Hz in the 10,000 and 100,000 Re data sets respectively. While the PIV data are not time resolved to smaller-scale motions, such as Kelvin-Helmholtz rollup of the shear layers, the frequency of the flapping is low enough to

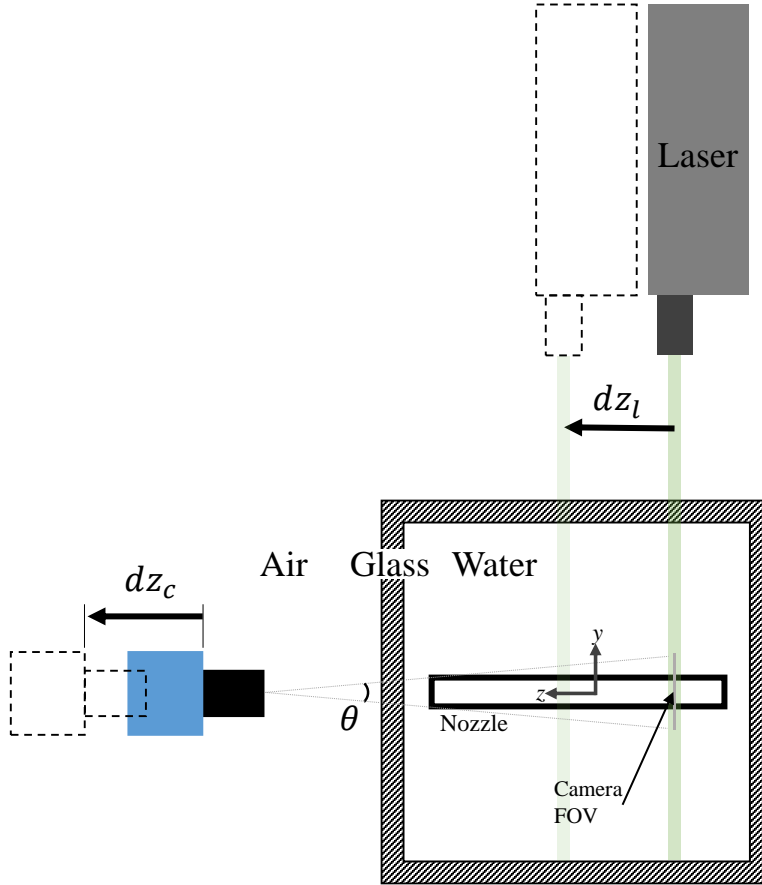


Fig. 4.5: Cross section view of nozzle illustrating a 2C PIV setup. To maintain a similar FOV between measurement planes, differences in the index of refraction mean the ratio of camera movement (dz_c) to laser movement (dz_l) are not 1:1.

determine the frequency with a resolution of 0.05 Hz. These events only affect the flow downstream of the exit and do not impact measurements at the jet exit. Additionally, these events are not visible in the flowmeter measurements, indicating that they do not impact the losses through the system.

4.2 Processing

The utility of various processing steps is first compared using the metrics of uncertainty, calculation time, and difference in volume-flow-rate from the best-case processing. All processing steps were compared using a single data set acquired at the $z = 0.00$ plane at $Re = 100,000$. As no single processing step can be used alone, combinations of processing steps are collected together in cases. Each case is identified with a four-digit number in the format of P####. Two cases are

used as benchmarks: P0001 and P0002. The first case, P0001, is heavily processed with no concern for calculation time and is considered the “best case” (BC). This case has the lowest instantaneous uncertainty and is considered the best value for comparison to other cases. The second case is a low-cost processing case that is used as a baseline to compare changes to processing steps. Table 4.2 provides a list of cases used for examining processing and acquisition parameters with a short description of the parameter that is varied. A comprehensive list of processing options for each case has been included in appendix A.

Table 4.2: Reference list of processing parameters giving a short description of what parameter is varied.

Name	Description	Name	Description
P0001	BC	P0027	PTV Intensity Threshold - 10000
P0002	Baseline	P0028	PTV Corr Window Size - 12
P0003	PreProcessing - PIN	P0029	PTV Allowed Vec Range - 1
P0004	PreProcessing - Sliding BG	P0030	PTV Allowed Vec Range - 3
P0005	IW Weighting(Both) - Round	P0031	PTV Median Filter
P0006	IW Weighting(Both) - 4:1	P0032	PTV Denoising - Avg 6
P0007	IW Weighting(2nd Only) - 4:1	P0033	PTV Denoising - Avg 6 / 1
P0008	IW Weighting(Both) - Adaptive	P0034	PTV Denoising - Poly2 6
P0009	IW Passes(1st) - 4	P0035	PTV Convert Grid - Avg 6 / 8 / 8
P0010	IW Passes(2nd) - 3	P0036	PTV Convert Grid - Poly2 6 / 8 / 8
P0011	IW Passes(2nd) - 4	P0037	GPU - Baseline
P0012	High Acc Final Pass - Y	P0038	GPU IW Weighting(Both) - Round
P0013	Multipass Corr. Func - std/norm	P0039	GPU IW Weighting(Both) - 4:1
P0014	Multipass Corr. Func - norm/norm	P0040	GPU IW Passes(2nd) - 4
P0015	Multipass Q ratio - 2.5	P0041	GPU - Reference Vector Field
P0016	Multipass Median Filter Passes - 3	P0042	GPU - Preprocessing - PIN
P0017	Multipass Rem/Reinsert Std - 1 / 2	P0043	SUM - Baseline
P0018	Post Vec Range - 10 ± 10 pix / 0 ± 5 pix	P0044	SUM Preprocessing - PIN/BG
P0019	Post Q ratio - 3	P0045	Mask of entire exit
P0020	Post Median Filter Passes - 3	P0046	Optimized for Flow Rate
P0021	PreProcessing - Butterworth Filter	P0047	Low Density - PPP = 0.004
P0022	Multipass Post Med Filt Passes - 5	P0048	Low Density - PPP = 0.006
P0023	IW Overlap (1st) - 75	P0049	Particle Displacement - 4 pix
P0024	IW Passes - 4 passes at smaller IW	P0050	Particle Displacement - 6 pix
P0025	PTV Intensity Threshold - 10	P0051	Particle Displacement - 13 pix
P0026	PTV Intensity Threshold - 1000		

All processing for investigations of the processing parameters, with the exception of GPU, was

performed on the same computer. Data were then normalized to the best case to generalize the calculation time results. GPU processing was performed on a computer with a similar processor in addition to a video card suitable for GPU processing (GeForce GTX960).

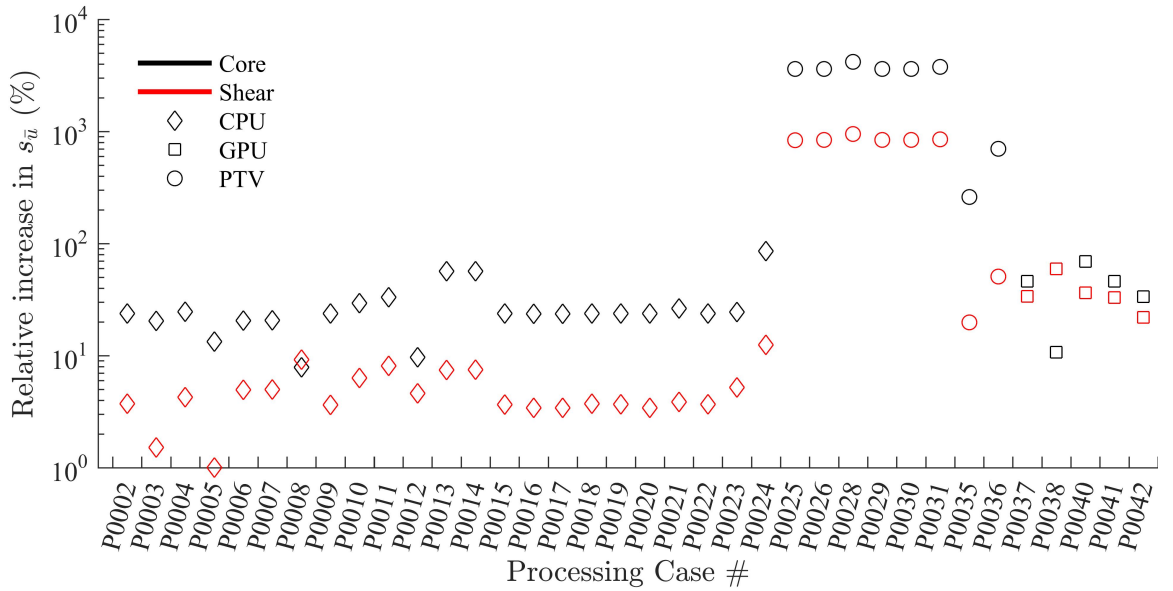


Fig. 4.6: Increases of random uncertainty for each processing case. Uncertainty is shown as a relative increase from BC processing (P0001). Absolute uncertainty in the shear is larger than uncertainty in the core.

Only the random uncertainty of the time-mean as determined by DaVis (Eq. 2.13) is used to compare processing parameters in Fig. 4.6. Uncertainty of the mean is reported as a percentage increase over the BC processing (P0001) which had uncertainty values of 0.0025 m/s in the core region and 0.0282 m/s in the shear region. Uncertainty is not shown for cases processed using the SUM method as it does not determine uncertainty of the mean, since this calculation requires the Reynolds stress. Processing cases using PTV that did not convert to a grid had the highest uncertainty. For comparison, the CPU case with the highest uncertainty, P0024, has an uncertainty increase close to 100% over P0001, while the PTV cases has uncertainty that is 800% of best case in the shear regions and 3600% in the core. Uncertainty in the core region varies more than in the shear region. Part of the variation is due to the small uncertainty in the core of the jet for the best-case.

DaVis only accounts for the time spent determining vector fields when reporting processing

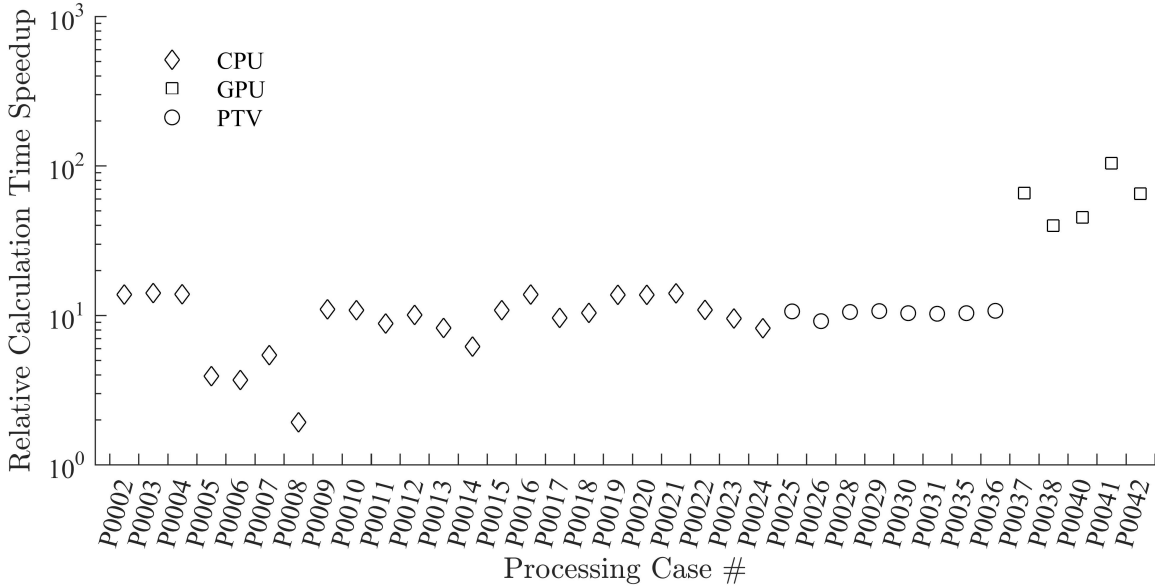


Fig. 4.7: Calculation time of each processing case. Calculation time is shown as a relative increase over the calculation time of BC processing (P0001).

time. This is a useful metric but is often an incomplete picture. Processing steps such as image preprocessing or filtering can be a significant portion of the total time spent processing. Processing techniques such as the sum of correlation (SUM) spend a trivial amount of time determining vector fields as the number of vector fields calculated is equal to the number of passes. Despite this, total calculation time is on the order of the slower CPU processing due to data transfer. Notably, all PIV+PTV processing cases using the de-noising filter were abandoned due to excessive calculation time. The “fastest” de-noising filter was run for 3 days with an estimated 5 additional days for completion. GPU processing was an average of 64 times faster than the BC case while the average CPU processing case was only 9.8 times faster than the BC. The BC had a processing time of 93,377 seconds (25h : 56m : 17s).

For the purposes of comparing processing cases, volume-flow-rate through the nozzle is determined by extrapolating the mean velocity profile at $z = 0$ over the entire exit plane. Processing cases are reported as deviations from the BC, which is assumed to be the most accurate. Almost all CPU processing changes had minimal impact on volume-flow-rate estimation. The exception is case P0013 which uses a high-accuracy final pass. Using this option corrects for a small bias which

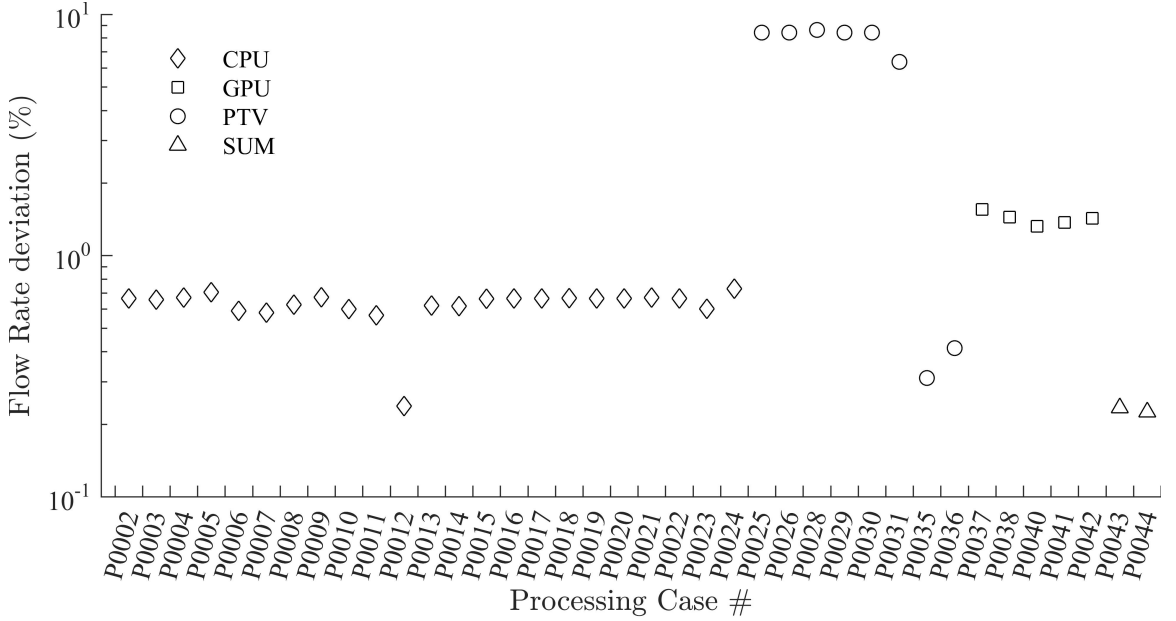


Fig. 4.8: Volume-flow-rate deviation from the BC for each processing case. Deviation is determined by the absolute difference in volume-flow-rate.

can be seen in Fig. 4.9. This velocity bias is about 0.6% of the mean flow.

In general PIV+PTV was the least accurate when compared to the BC with a deviation of 7%. PTV vector fields converted to a grid (P0035 and P0036), is one of the better options with a deviation of 0.3%. GPU processing has an average deviation of 1.4%. CPU processing has a deviation of 0.6%. The SUM method had the least amount of deviation at 0.2%.

The time required for preprocessing images is not recorded by Davis. Particle Image Normalization (PIN) as preprocessing was examined in cases P0003 and P0042. PIN is one of the more effective options to decrease uncertainty over the baseline cases for both CPU and GPU processing. It also reduced the amount of volume-flow-rate deviation from the BC. Background subtraction was examined in cases P0004 and P0044 and slightly increased uncertainty for both cases. Sliding background subtraction was enabled by default for all GPU cases and could not be turned off. A Butterworth was used in case P0021 and had little to no effect on uncertainty or volume-flow-rate measurements.

The effects of IW weighting are examined in cases P0005-P0008 for CPU and cases P0037-P0038 for GPU. For random uncertainty of the time-mean velocity, round weighting performed

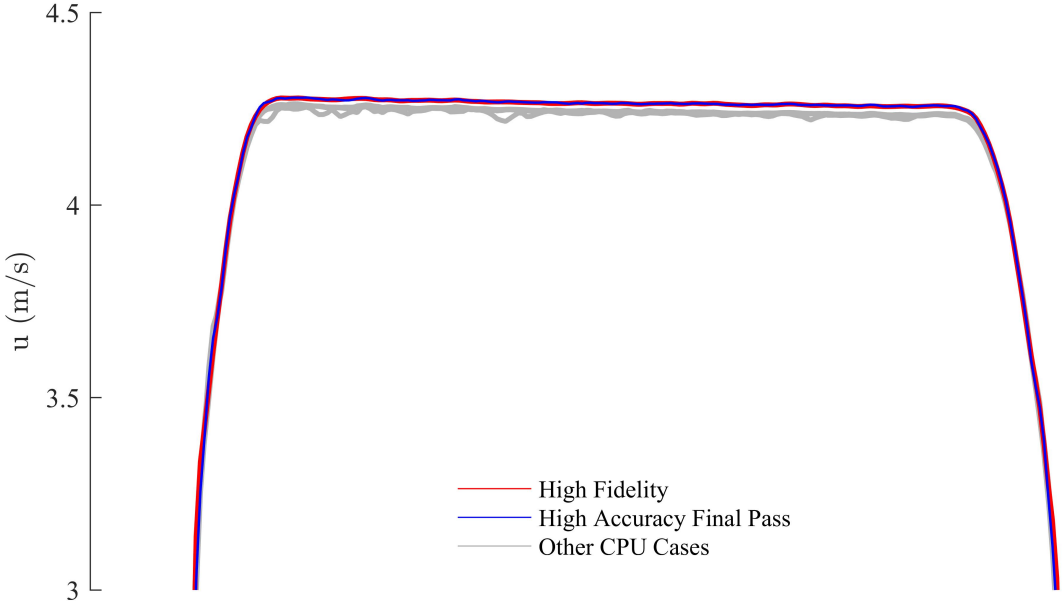


Fig. 4.9: Velocity profiles for all of the CPU processed cases. Only the case processed using the high-accuracy final pass option and the BC processing are in color to illustrate the velocity bias.

better than elliptical 4:1 weighting, which performed marginally better than no weighting. The use of any weighting significantly increases calculation time. Both round and 4:1 elliptical weighting were only four times faster processing than the BC while the baseline case with no weighting was 14 times faster.

Some of the improved calculation time may be offset by only using weighting on the second pass. Cases P0006 and P0007 produced nearly identical results for uncertainty and volume-flow-rate deviation but only P0006 used IW weighting for both passes while P0007 only used IW weighting for the final pass.

Circular weighting for GPU processing (P0038) produced the lowest uncertainty of the mean in the core region but significantly higher uncertainty in the shear region. The processing case for GPU 4:1 elliptical weighting was not processed as the DaVis software would crash. Software updates were unable to correct this issue.

Adaptive windows are expected to produce the lowest uncertainty. Fig. 4.6 shows that adaptive IW, P0008, has the largest random uncertainty of the mean in the shear region. Fig. 4.10 shows that the random instantaneous uncertainty in the shear region decreases. This implies that adaptive win-

dows are better resolving small flow fluctuations. This lowers the instantaneous random uncertainty but increases the standard deviation.

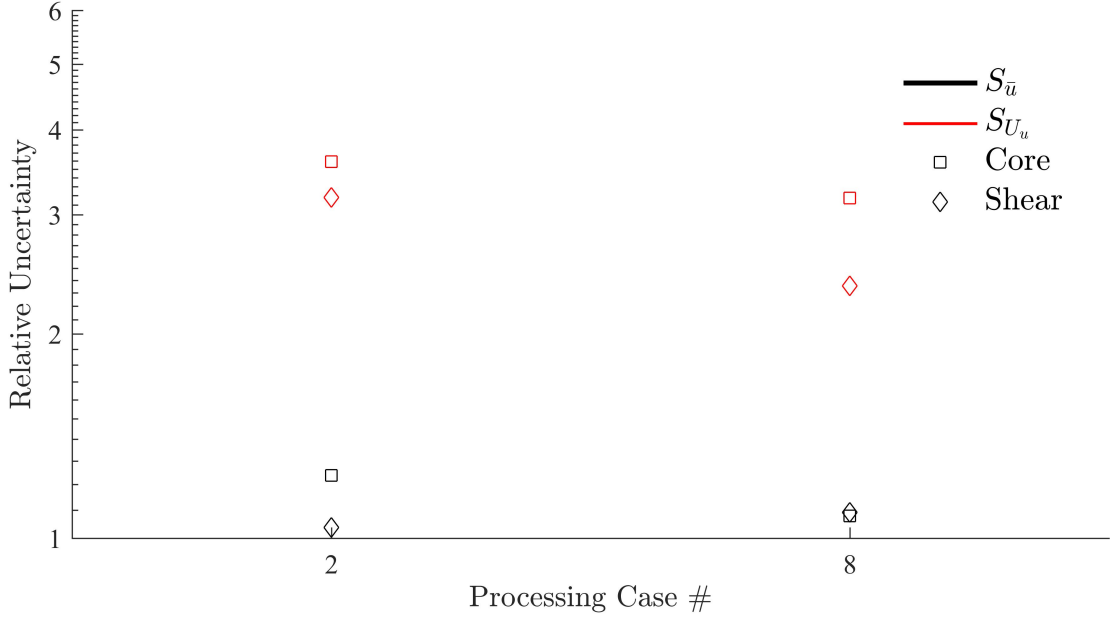


Fig. 4.10: Random uncertainty of the mean and random instantaneous uncertainty of the baseline processing case, P0002 and the processing case for adaptive IW, P0008. Data in black is the random uncertainty of the mean from Fig. 4.6.

The effects of the number of IW passes are examined in cases P0009-P0011 and P0024. Increasing the number of the initial passes has little effect on uncertainty of the mean while increasing the number of final passes from two to three and four, cases P0002, P0010 and P0011 respectively, increases uncertainty of the mean in both the core and shear regions. Fig. 4.11 shows that random instantaneous uncertainty had a large decrease with three passes and smaller increase with the four passes. This indicates that more passes better resolves small flow fluctuations. Large increases in uncertainty of the mean are shown in case P0024 where the number of total passes remains the same at four, but without any initial passes. The effect of the number of IW passes on volume-flow-rate deviation was small as seen in Fig. 4.8.

Normalizing the correlation field as a multi-pass option is examined in cases P0013-P0014. It results in a large increase in the random uncertainty of the mean. Fig. 4.11 shows that random instantaneous uncertainty decreases and is better resolving small flow fluctuations. Volume-flow-rate

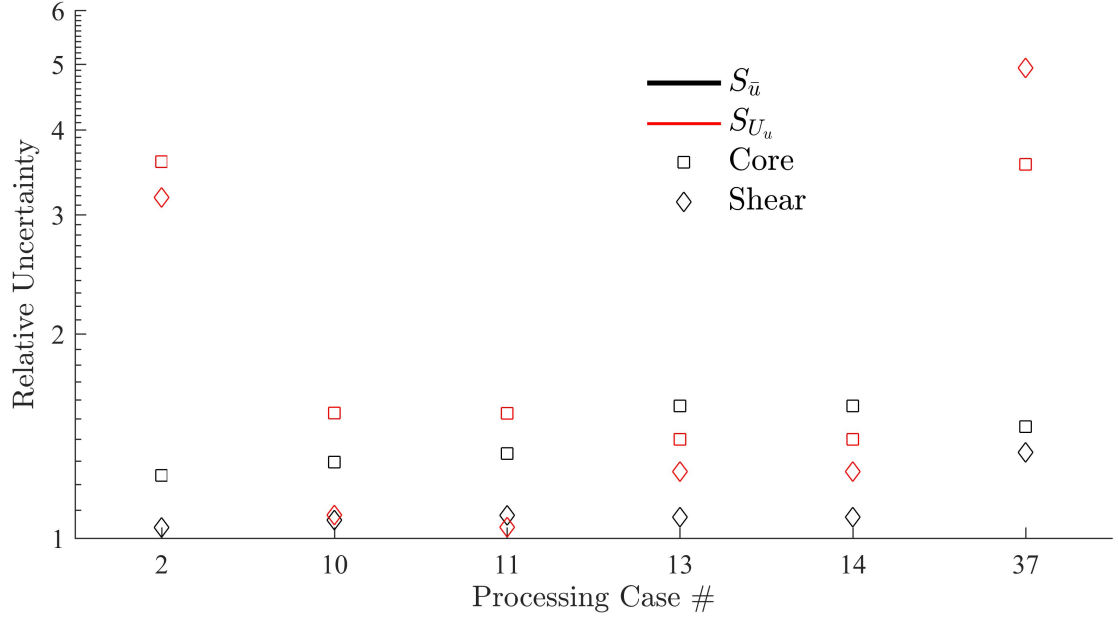


Fig. 4.11: Random instantaneous uncertainty, in blue, plotted with the random uncertainty of the mean from Fig. 4.11 for selected processing cases.

deviation was not affected. This scheme is calculation intensive, more than doubling the processing time compared to the base-line case. Normalizing both the initial and final passes showed almost no improvement over normalizing only the final pass. This processing scheme had minimal effect on volume-flow-rate deviation.

Processing steps P0015-P0023 examine the effects of different post-processing schemes, both for multi-pass post-processing and final post-processing. Their effects on uncertainty, volume-flow-rate deviation, and calculation time are minimal. We posit that these options would have more effect on data of lower quality.

The use of a reference field in GPU processing provides a large improvement in calculation time. The baseline GPU processing was 66 times faster than the high fidelity case. Using a reference vector field to reduce the initial search area allowed for vector calculations to be performed 104 times faster for almost identical uncertainties and a slight improvement in volume-flow-rate deviation.

In general, GPU processing has larger random uncertainty of the mean. Fig. 4.11 shows the standard deviation of the random instantaneous uncertainty for the baseline GPU processing,

P0037. GPU processing should produce identical results to CPU processing. Random instantaneous uncertainty in the core region remains similar. However, random instantaneous uncertainty in the shear region increased with GPU processing. We note that all GPU processing enables a sliding background as a preprocessing step that cannot be disabled and that Q-ratio (which is the ratio of the largest correlation peak to the next largest and should not to be confused with volume volume-flow-rate) is not available as a metric of quality of the vector in post-processing. The use of a sliding background is shown to slightly increase random uncertainty of the mean in case P0004. In place of a Q-ratio, a minimum correlation value was used. It is unclear if these processing changes account for the relative large increase in the random uncertainty of the mean. The increase in the random instantaneous uncertainty suggests that better resolving small fluctuations in the flow is not the primary reason for the increase in random uncertainty of the mean.

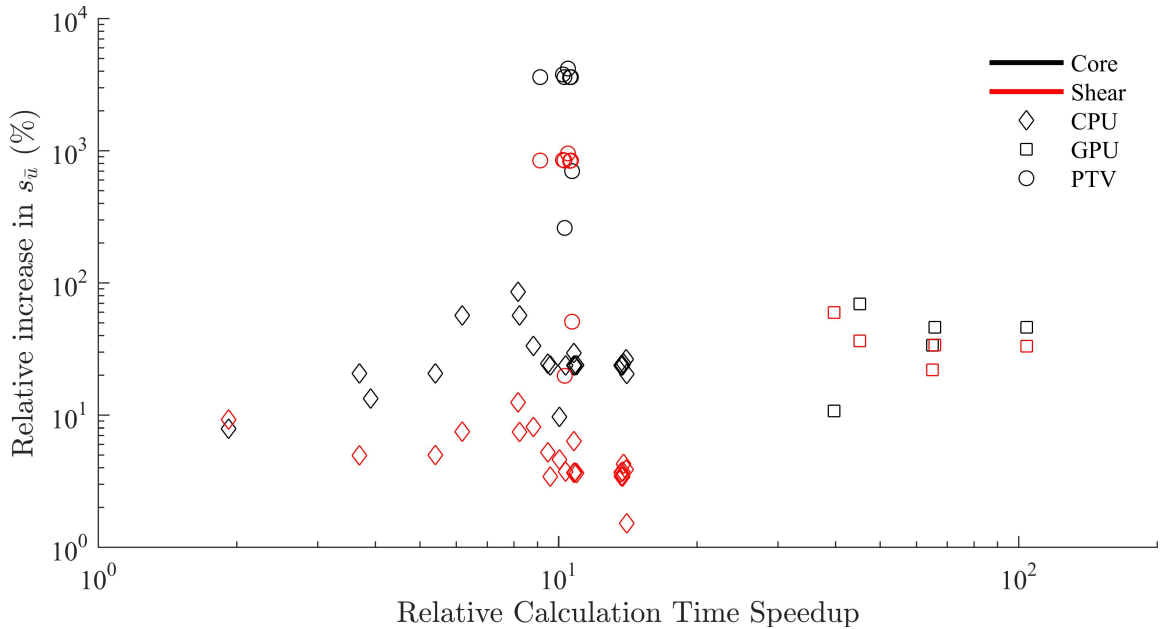


Fig. 4.12: Random uncertainty increase versus calculation time. The lower right portion of the figure is the ideal location representing low uncertainty and fast calculation time.

Fig. 4.12 shows the trade-offs between uncertainty and calculation time. Both CPU and GPU processing have several points with similar uncertainty but different calculation times. This illus-

trates that choosing more computationally intensive processing options does not necessarily translate into better results.

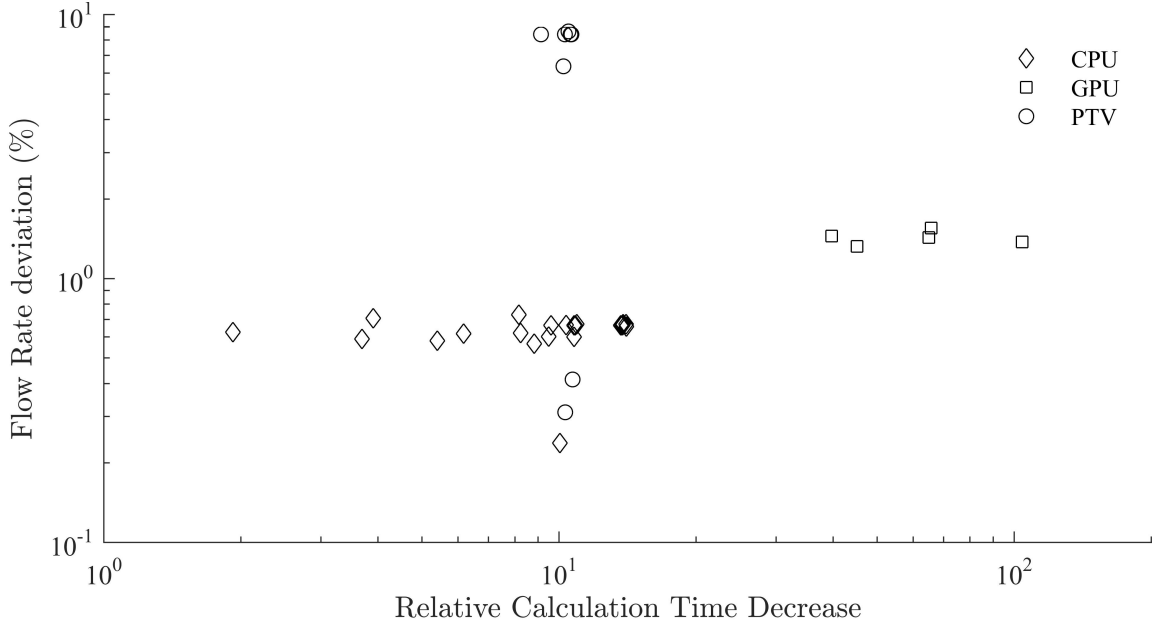


Fig. 4.13: Volume-flow-rate deviation and calculation time. The ideal location of the figure is the lower right portion indicating a volume-flow-rate close to the BC processing and fast calculation time.

Fig. 4.13 shows the trade-offs between volume-flow-rate deviation and calculation time. Unlike uncertainty, there is much less variation in volume-flow-rate for different processing options. The exception is data processed through PIV+PTV, which varies little in calculation time but has considerable volume-flow-rate deviation.

4.2.1 Processing Recommendations

For the purposes of measuring volume-flow-rate through a planar nozzle using PIV, we make the following data processing recommendations: Assuming the raw particle images are free from major defects and have sufficient seeding density and dynamic velocity range, Particle Image Normalization reduced random uncertainty of the mean better than a sliding background subtraction or Butterworth filter but no preprocessing significantly impacted volume-flow-rate deviation.

All processing should use a high-accuracy final pass. This one option accounts for the largest improvement for uncertainty and volume-flow-rate deviation.

For CPU processing, using round IW weighting produces the lowest random uncertainty of the mean and is otherwise comparable to 4:1 elliptical weighting. Adaptive weighting reduced random instantaneous uncertainty but at a heavy computational cost taking twice the calculation time of round or 4:1 elliptical IW weighting. No IW weighting can be used for the initial pass for a large improvement in calculation time and almost no effect on uncertainty or volume-flow-rate deviation. Using two initial and three final passes is sufficient to effectively reduce uncertainty of the mean. However, increasing the number of passes has less than 0.1% improvement in volume-flow-rate deviation.

Normalizing the correlation function is computational intensive but decreases uncertainty. It has little effect on flow-rate deviation. If used to reduce uncertainty, it should only be used on the final pass.

Post-processing, including multi-pass post-processing, showed little to no effect on uncertainty of the mean or volume-flow-rate deviation. GPU processing was up to two orders of magnitude faster than CPU processing but produced higher random uncertainty of the mean and higher instantaneous uncertainty. It also produced significantly higher volume-flow-deviation. A reference vector field should always be used for calculation time improvement.

PIV+PTV processing, when converted to a vector grid similar to a PIV vector field, produces higher random uncertainties but smaller volume-flow-rate deviation than CPU and GPU processing. PIV+PTV should not be used without conversion to a grid or some other treatment not explored by this report.

The sum of correlation method could not be evaluated based upon random uncertainty or calculation time but produces the lowest volume-flow-rate deviation. A very coarse calculation time can be estimated using file creation time stamps and places it about two times faster than the high fidelity case. This method is unique in that loading images from hard disk is the bulk of the calculation time. The hard drive used for this study has a nominal read speed of 30 MB/s. SSD hard drives can reach speeds of 1100 MB/s. A RAID0 configurations of four SSD hard drives can reach speeds

of 175,000 MB/s. While faster hard drive speeds will not translate 1:1 to faster calculation times, hard drive speed is the limiting factor on calculation time using the SUM method for this report. If only the mean flow is required, the SUM method has potential to be similar in calculation speed to GPU processing.

4.3 PIV Data Acquisition Parameters

The impact of how two PIV data acquisition parameters are now accessed using the metrics of uncertainty and difference in volume-flow-rate in comparison to the BC processing. Data were acquired with PPP equivalent to 4 and 6 particles per IW and for varying particle displacement of 4, 6, and 13 at the $z = 0$ location. Nominal values of PPP and particle displacement were 11 and 10 respectively.

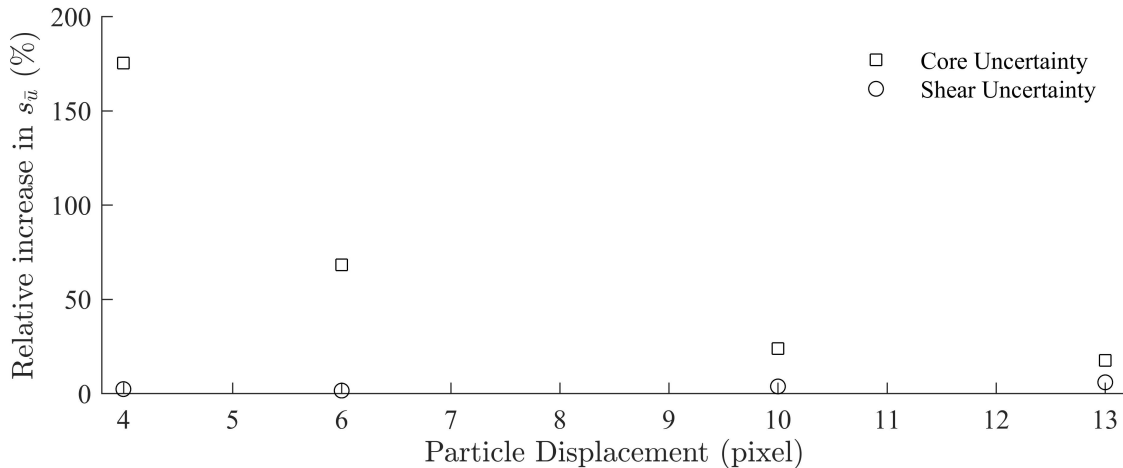


Fig. 4.14: Random uncertainty of the velocity mean versus particle displacement. A larger particle displacement results in a larger dynamic velocity range, which decreases instantaneous random uncertainty. Result at a particle displacement of 10 pixels is from the baseline processing case P0002.

Data were acquired for 3 different values of particle displacement between image pairs. Increasing particle displacement improves the dynamic velocity range. Having low dynamic velocity range increases random uncertainty (Fig. 4.14) and volume-flow-rate deviation (Fig. 4.15). Data using larger displacement shows a small decrease of core uncertainty, a small increase in shear

uncertainty, and increased volume-flow-rate deviation. Nominal pixel displacements for data acquisition was 10 pixels.

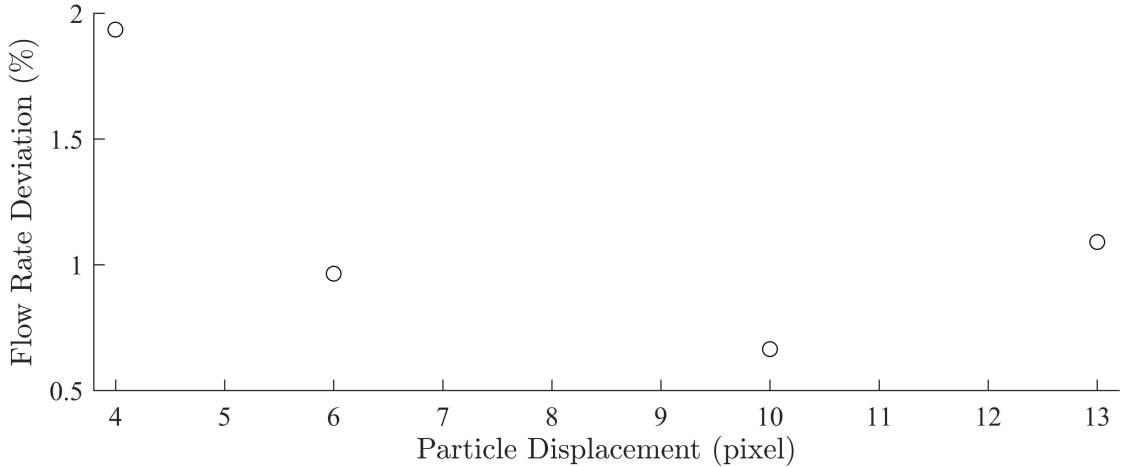


Fig. 4.15: Volume-flow-rate deviation versus particle displacement. Larger particle displacements result in a larger velocity dynamic range. Result at a particle displacement of 10 pixels is from the baseline processing case P0002.

Similar to the particle displacement data, the effect of low seeding density is to increase both uncertainty (Fig. 4.16) and volume-flow-rate deviation (Fig. 4.17). Increasing particle displacement has nominal effect on uncertainty of the mean but increase volume flow rate deviation. Large displacements can increase through-plane motion, causing loss of particle-pairs between images, or the flow may be starting to roll up. It is unclear what the cause is and recommend that future work explore this further.

Masking the exit of the nozzle produced no change from the baseline case for both uncertainty and volume-flow-rate deviation. All processing to compare data acquisition parameters was done using processing case P0002.

4.3.1 Data Acquisition Recommendations

Data acquisition parameters to best determine volume-flow-rate should follow the general PIV recommendations for quality data [5]. Both sufficient particle density and sufficient dynamic range are required for quality measurements.

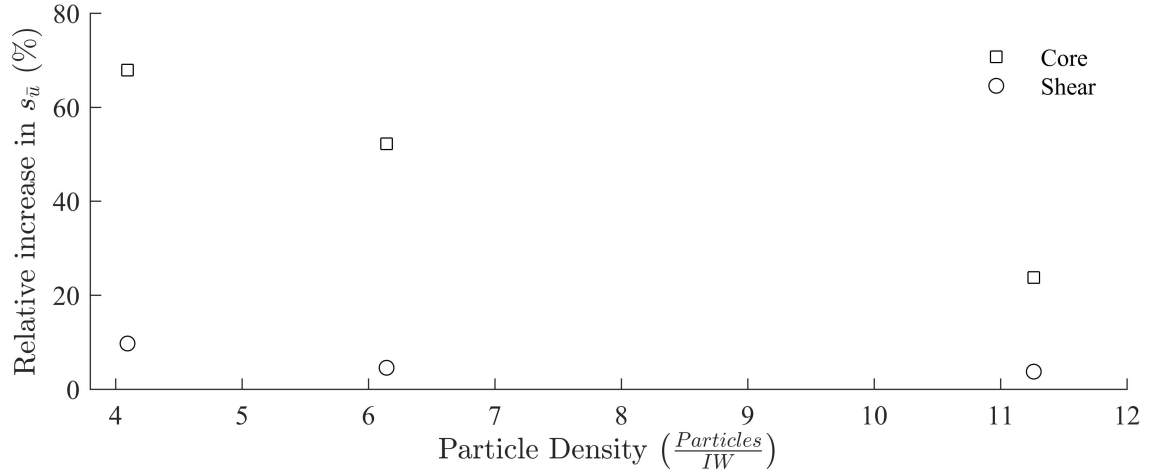


Fig. 4.16: Random uncertainty versus particle density. The probability of a valid vector increases with particle density, with diminishing returns after 8 particles in each IW. Results closest to 11 particles per IW is from baseline processing case P0002.

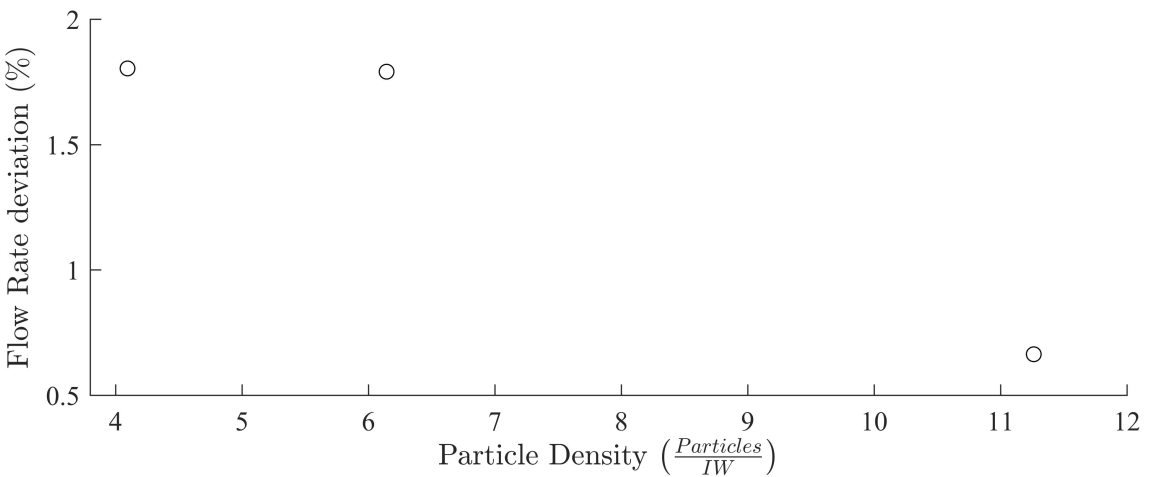


Fig. 4.17: Volume-flow-rate deviation versus particle density. Insufficient particle density increases volume-flow-rate deviation. Result closest to 11 particles per IW is from baseline processing case P0002.

4.4 Volume-Flow-Rate Measurements

Data were acquired at three Reynolds numbers for the purposes of comparing volume-flow-rate as calculated by PIV and the flow meter. Volume-flow-rates for all three Reynolds numbers of data were underestimated by 2C PIV compared to the magnetic flow meter by 6%. This means that the error scales with velocity and is much larger than predicted by our uncertainty analysis. A comprehensive analysis of possible reasons led to discovery of a leak between the jet inlet exterior and a baffle plate that supports the nozzle inlet as shown in Fig. 4.18. Bypass flow at this location would cause the meter to read higher than the PIV by an amount that scales with velocity.

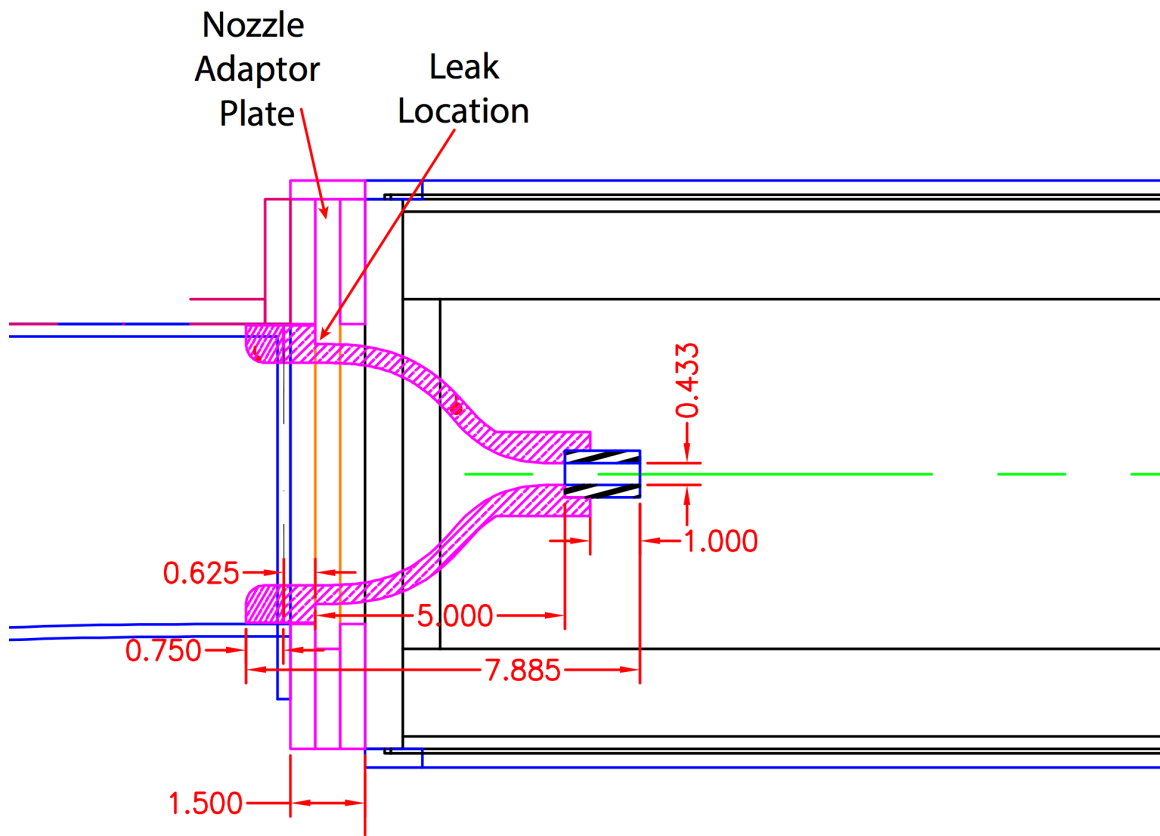


Fig. 4.18: Location of the leak. Water may be moving around the outside of the nozzle and the nozzle adapter plate. This flow is measured by the flow meter but not PIV measurements.

As this leak was noticed after measurement equipment had been reset for stereo PIV acquisition, it was decided to assess the amount of the leak through stereo PIV data acquired before and after repair. Repair of the leak decreased error by 1.97%. Two-component PIV data is reported as measured and with an adjustment to compensate for the amount of error that can be attributed to the leak.

4.4.1 Volume-Flow-Rate From 2C PIV

Results from section 4.2 were used to guide selection of processing parameters used to measure volume-flow-rate. Specific processing options are found in case P0046.

Two methods are used to spatially integrate the five measurement planes for each Reynolds number. Both methods use the trapezoid rule and vector location to integrate each velocity profile in the y -dimension. The first method uses the trapezoid rule in the z -dimension over the long dimension of the nozzle, W . Seven planes in total are used: the five measurement plane locations and $\pm W/2$ locations where velocity values are set to 0.

The second method uses knowledge of the laser sheet thickness and information from shakedown to proportionally assign volume-flow-rate to measurement planes. PIV measurements are spatially averaged over the volume of the laser sheet. Profiles obtained from shakedown show that in-plane velocity gradients at the $\pm W/2$ locations are too high to resolve. Measurement planes located at 52.9 mm were chosen to be in the core of the flow but near the shear layer. However, due to the Gaussian nature of laser beams (and thus sheets) the measurement plane could not be completely isolated from particles in the shear layer. The trapezoid rule sums by averaging two points and multiplying it by the distance between them, giving equal weight to both points. Using the trapezoid rule between the measurement planes at $z = 0.0$ mm and $z = \pm 52.9$ mm allows particles in the shear layer, that influenced the measurement plane at $z = \pm 52.9$ mm, to influence calculations for flow far away from the shear layer. At this location the measurement plane location is located at the edge.

The proportional method assigns each measurement plane a percentage of W . This assigns the most weight to the $z = 0.00$ mm measurement plane which best represents the core of the flow.

Locations of measurement planes are plotted over a velocity profile from shakedown in Fig. 4.19.

For each Reynolds number, volume-flow-rate was estimated by numerically integrating the 5 measurement planes using both the trapezoid and proportional methods. For both integration methods, the limits of integration are chosen where velocity goes to zero at the edges of the velocity profile. Results are shown in Table 4.3.

Table 4.3: Results of volume-flow-rate measurements using 2C PIV. Negative values indicate measurements made by PIV were less than the flow meter. Values in parentheses are adjusted for nozzle leak.

Reynolds Number	Error	
	Trapezoid Rule	Proportional
100,000	-6.14% (-4.17%)	-5.25% (-3.28%)
75,000	-6.00% (-4.03%)	-4.99% (-3.02%)
10,000	-5.10% (-3.13%)	-0.28% (1.69%)

4.4.2 Volume-Flow-Rate From Stereo PIV

The increased amount of information in the z -dimension of stereo data simplifies integration. All data were processed using options to minimize uncertainty and volume-flow-rate deviation with complete list of processing specified in processing case P0046. Tab 4.4 shows the results of using stereo PIV to measure volume-flow-rate. The two turbulent measurements are 2% off of the flow meter.

Table 4.4: Results of volume-flow-rate measurements made using stereo PIV. Negative values indicate measurements made by PIV were less than the flow meter.

Reynolds Number	Error
100,000	-2.08%
75,000	-2.03%
10,000	-1.58%

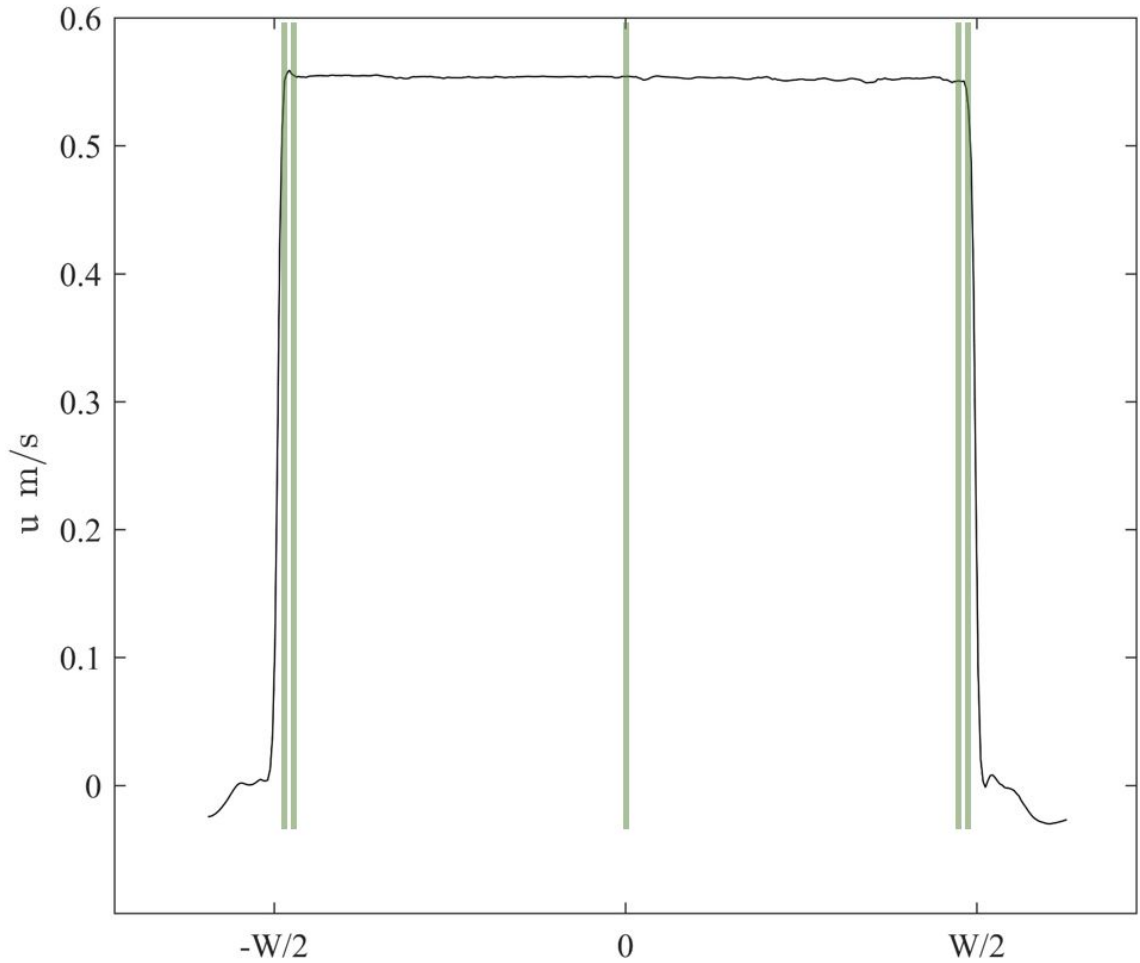


Fig. 4.19: Locations of profiles in the x - y plane that are used to calculate volume-flow-rate. Vertical green bars are representative of the location of each measurement plane and thickness of the laser sheet. They are plotted over a velocity profile for $\text{Re} = 10,000$ in the x - z plane. The profile data are from shakedown. A limited number of measurement planes are used to represent the entire profile, with each containing information only from the measurement plane. Information about the flow between measurement planes is interpolated using information from the two bounding measurement planes. Integration using the trapezoid rule assigns equal weight to each of the bounding measurement planes.

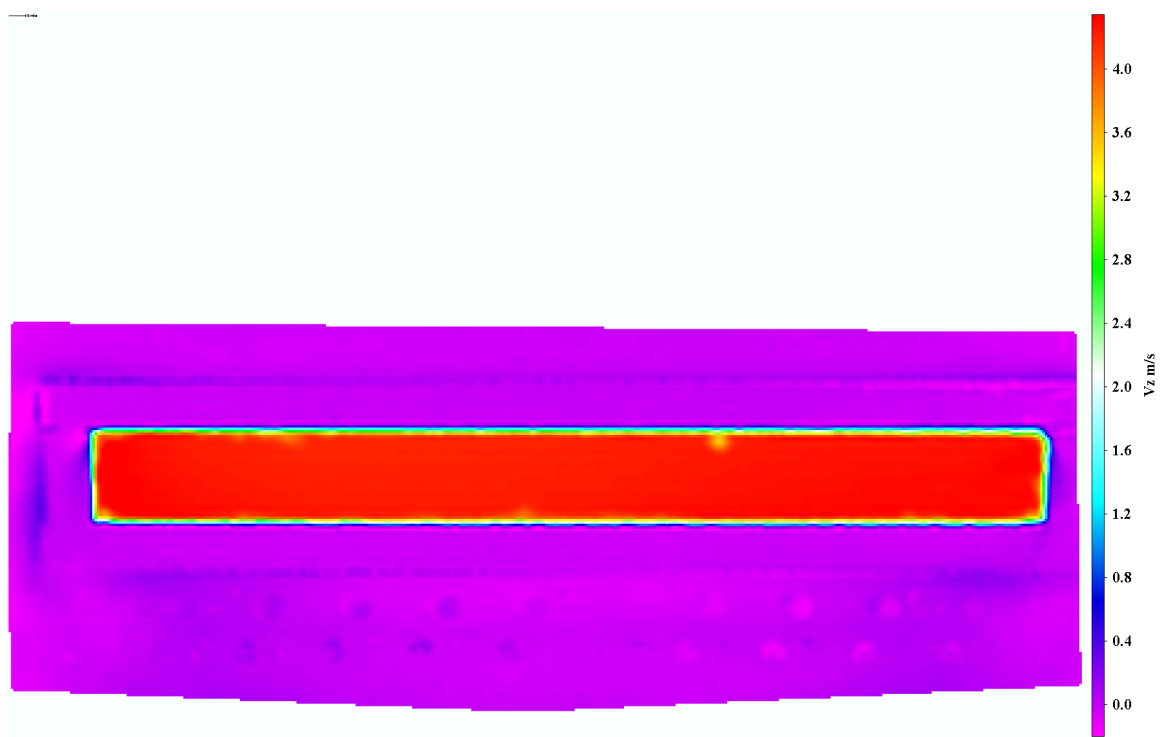


Fig. 4.20: Average streamwise velocity of a Stereo PIV measurement at $\text{Re} = 100,000$.

CHAPTER 5

Conclusions

The goals of this work were to assess a range of data acquisition and processing parameters for measuring volume flow rate through a rectangular nozzle using PIV. The effects of these parameters were examined by systematically changing parameters one at a time and evaluating difference in uncertainty, calculation time, and volume flow rate deviation.

The data acquisition parameters that were varied included particle density, particle displacement, and masking of the exit plane. The effects of particle density and displacement followed the trends of previous work in that insufficient density and sub-optimal particle displacement increased uncertainty and negatively affected flow rate measurements.

A multitude of processing parameters were varied for CPU, GPU, Sum of Correlation, and PTV+PIV processing methods. Recommendations for each method are developed and listed with potential drawbacks. All processing should use a high-accuracy final pass. Using two initial passes and three final passes is sufficient for quality data. No IW weighting can be used for the initial pass for a large improvement in calculation time with almost no drawbacks. PIV+PTV processing should be converted to a vector grid similar to a PIV vector field. A reference field should always be used for GPU processing.

Flow rates for three Reynolds numbers are determined through 2C PIV data at five measurement planes and compared to a flow meter. Volume flow rates using 2C PIV were found to underestimate flow by 3-4%.

Flow rates for three Reynolds numbers are determined through stereo PIV data and compared to a flow meter. Volume flow rates using stereo PIV were found to underestimate flow by 2%.

REFERENCES

- [1] van Doorne, C. W. H. and Westerweel, J., “Measurement of laminar, transitional and turbulent pipe flow using Stereoscopic-PIV,” *Experiments in Fluids*, Vol. 42, No. 2, 2007, pp. 259–279. doi:10.1007/s00348-006-0235-5.
- [2] Pope, S. B., *Turbulent Flows*, Cambridge University Press, 2015.
- [3] Lozanova, M. and Stankov, P., “Experimental investigation on the similarity of a 3D rectangular turbulent jet,” *Experiments in Fluids*, Vol. 24, 1998, pp. 470–478. doi:10.1016/s0017-9310(03)00155-8.
- [4] Prasad, A. K., “Stereoscopic particle image velocimetry,” *Experiments in Fluids*, Vol. 29, Feb 2000, pp. 103–116.
- [5] Adrian, R. J. and Westerweel, J., *Particle Image Velocimetry*, Cambridge University Press, New York, New York, 1st ed., 2011.
- [6] Adrian, R. J., “Hairpin Vortex Organization in Wall Turbulence,” *Physics of Fluids*, Vol. 19, No. 4, 2007, pp. 041301. doi:10.1063/1.2717527.
- [7] Keane, R. D. and J., A. R., “Theory of cross-correlation analysis of PIV images,” *Applied Scientific Research*, Vol. 49, July 1992, pp. 191–215.
- [8] Timmins, B. H., *Automatic Particle Image Velocimetry Uncertainty Quantification*, Master’s Thesis, Utah State University, 2011.
- [9] Wilson, B. M. and Smith, B. L., “Uncertainty on PIV mean and fluctuating velocity due to bias and random errors.” *Measurement Science and Technology*, Vol. 24, No. 3, 2013, pp. 15.
- [10] Kähler, C. J., Astarita, T., Vlachos, P. P., Sakakibara, J., Hain, R., Discetti, S., La Foy, R., and Cierpka, C., “Main results of the 4th International PIV Challenge,” *Experiments in Fluids*, Vol. 57, No. 6, 2016, pp. 97. doi:10.1007/s00348-016-2173-1.
- [11] LaVision GmbH, *FlowMaster Product Manual, Item Number: 1105011-4*, LaVision GmbH, Anna-Vandenhoeck-Ring 19, D-37081 Göttingen, Germany, Mar 2015.
- [12] LaVision GmbH, *DaVis 8.3 Software Manual, Item Number: 1105xxx*, LaVision GmbH, Anna-Vandenhoeck-Ring 19, D-37081 Göttingen, Germany, Mar 2015.
- [13] Scarano, F. and Sciacchitano, A., *Robust Elimination of Light Reflections in PIV*, s.n., 2011, pp. 1–7.
- [14] Willert, C., “Stereoscopic digital particle image velocimetry for application in wind tunnel flows,” *Measurement Science and Technology*, Vol. 8, No. 12, 1997, pp. 1465.
- [15] Wieneke, B., “Stereo-PIV using self-calibration on particle images,” *Experiments in Fluids*, Vol. 39, No. 2, 2005, pp. 267–280. doi:10.1007/s00348-005-0962-z.

- [16] Mi, J., Deo, R. C., and Nathan, G. J., “Characterization of turbulent jets from high aspect ratio rectangular nozzles,” *Physics of Fluids*, Vol. 17, No. 6, 2005.
- [17] Quinn, W., “Turbulent free jet flows issuing from sharp-edged rectangular slots: The influence of slot aspect ratio,” *Experimental Thermal and Fluid Science*, Vol. 5, No. 2, 1992, pp. 203 – 215. doi:[http://dx.doi.org/10.1016/0894-1777\(92\)90007-R](http://dx.doi.org/10.1016/0894-1777(92)90007-R).
- [18] Quinn, W., “Development of a large-aspect-ratio rectangular turbulent free jet,” *AIAA Journal*, Vol. 32, No. 3, 1994, pp. 547–554.
- [19] Westerweel, J., “Fundamentals of digital particle image velocimetry,” *Measurement Science and Technology*, Vol. 8, No. 12, 1997, pp. 1379.
- [20] Lecordier, B., Demare, D., Vervisch, L. M. J., RÃ©veillon, J., and TrinitÃ©, M., “Estimation of the accuracy of PIV treatments for turbulent flow studies by direct numerical simulation of multi-phase flow,” *Measurement Science and Technology*, Vol. 12, No. 9, 2001, pp. 1382.
- [21] Sciacchitano, A., Neal, D. R., Smith, B. L., Warner, S. O., Vlachos, P. P., Wieneke, B., and Scarano, F., “Collaborative Framework for PIV Uncertainty Quantification: Comparative Assessment of Methods,” *Measurement Science and Technology*, Vol. 26, No. 7, 2015, pp. 1–15. doi:[10.1088/0957-0233/26/7/074004](https://doi.org/10.1088/0957-0233/26/7/074004).
- [22] Coleman, H. W. and Steele, W. G., *Experimentation, Validation, and Uncertainty Analysis for Engineers*, John Wiley and Sons, Hoboken, NJ, 3rd ed., 2009.
- [23] Wieneke, B., “PIV uncertainty quantification from correlation statistics,” *Measurement Science and Technology*, Vol. 26, No. 7, 2015, pp. 10.
- [24] Sciacchitano, A., Wieneke, B., and Scarano, F., “PIV uncertainty quantification by image matching,” *Measurement Science and Technology*, Vol. 24, No. 4, 2013, pp. 16.
- [25] Sciacchitano, A. and Wieneke, B., “PIV uncertainty propagation,” *Measurement Science and Technology*, Vol. 27, No. 8, 2016, pp. 084006.
- [26] Thormählen, I., Straub, J., and Grigull, U., “Refractive Index of Water and Its Dependence on Wavelength, Temperature, and Density,” *Journal of Physical and Chemical Reference Data*, Vol. 24, 1985, pp. 933–945. doi:[10.1063/1.555743](https://doi.org/10.1063/1.555743).
- [27] Song, H. B., Yoon, S. H., and Lee, D. H., “Flow and heat transfer characteristics of a two-dimensional oblique wall attaching offset jet,” *International Journal of Heat and Mass Transfer*, Vol. 43, No. 13, 2000, pp. 2395 – 2404.

APPENDICES

Appendix A

Processing Parameters

				<u>P0001</u>	<u>P0002</u>	<u>P0003</u>	<u>P0004</u>
		Notes	Best Case	Base line			
Time	Type		Butterworth	-	-	-	-
Filter	# Images		9	-	-	-	-
	Preprocessing	P.I.N.	24	-	24	-	
		Sliding BG Size	8	-		8	
	Define Mask		Geometric	Geometric	Geometric	Geometric	
		Size	64	64	64	64	
	Pass 1	Weight	4:1 (1)	square	square	square	
		Overlap	50	50	50	50	
		Passes	4	2	2	2	
		Size	32	32	32	32	
	Pass 2	Weight	Auto	square	square	square	
		Overlap	75	75	75	75	
		Passes	6	2	2	2	
	High Acc Final Pass		Y	N	N	N	
PIV	Vector Calc	GPU	Pass 1	-	-	-	-
			Pass 2	-	-	-	-
			Pass 3	-	-	-	-
			All further	-	-	-	-
	Multipass options	Ref Vector Field	AvgV	-	-	-	-
		Corr. Initial	Normalized	standard	standard	standard	standard
		Corr. Final	Normalized	standard	standard	standard	standard
		Deformed IW	Symmetric	Symmetric	Symmetric	Symmetric	Symmetric
		Q Ratio	3	1.2	1.2	1.2	1.2
	Multipass Postprocessing	Median Filter	r&i r	r&i r	r&i r	r&i r	r&i r
		Type # Times	5	1	1	1	1
		Remove std	1	1.5	1.5	1.5	1.5
		Reinsert Std	1.2	2.5	2.5	2.5	2.5
		Remove Groups <	5	5	5	5	5
	Postprocessing	Vec Range	vx	-	-	-	-
			vy	-	-	-	-
		Q Ratio<	2	2	2	2	2
		Type # Times	r&i r	r&i r	r&i r	r&i r	r&i r
		Median Filter	4	1	1	1	1
			2	2	2	2	2
		Remove Std	3	3	3	3	3
		Reinsert Std	5	5	5	5	5
		Remove Groups <					

		Notes		P.I.N.	P0025	P0026	
		Sliding BG		Size	-	-	
				Size	64	64	
		Pass 1		Weight	square	square	
				Overlap	50	50	
				Passes	2	2	
				Size	32	32	
		Pass 2		Weight	square	square	
				Overlap	75	75	
				Passes	2	2	
		High Acc Final Pass		N	N	N	
		Vector Calc		Ref Vector Field	-	-	
		Multipass options		Corr. Initial	standard	standard	
				Corr. Final	standard	standard	
				Deformed IW	Asymmetric	Asymmetric	
				Q Ratio	1.2	1.2	
PIV+PTV			Postprocessing	Type	r&i r	r&i r	
				Median	1	1	
				Filter	1.5	1.5	
				Remove std	2.5	2.5	
				Reinsert Std			
				Remove Groups <	5	5	
		Particle Detection		Particle Size Range	2-6	2-6	
				Intensity Threshold	10	1000	
		PTV Calc		Correlation and	8	8	
				Matching	2	2	
				Allowed vec range			
		Median Filter		Type	-	-	
				# Times	-	-	
				Remove Std	-	-	
				Reinsert Std	-	-	
		PTV Post-Processing		Type	-	-	
				# of vec	-	-	
		Denoising Filter		Ignore N outliers	-	-	
				Type	-	-	
		Convert to Grid		# vec	-	-	
				Grid size	-	-	
				Disable Range	-	-	

	<u>P0027</u> PIV+PTV	<u>P0028</u> PIV+PTV	<u>P0029</u> PIV+PTV	<u>P0030</u> PIV+PTV	<u>P0031</u> PIV+PTV	<u>P0032</u> PIV+PTV	<u>P0033</u> PIV+PTV
-	-	-	-	-	-	-	-
-	-	-	-	-	-	-	-
64	64	64	64	64	64	64	64
square	square	square	square	square	square	square	square
50	50	50	50	50	50	50	50
2	2	2	2	2	2	2	2
32	32	32	32	32	32	32	32
square	square	square	square	square	square	square	square
75	75	75	75	75	75	75	75
2	2	2	2	2	2	2	2
N	N	N	N	N	N	N	N
-	-	-	-	-	-	-	-
standard	standard	standard	standard	standard	standard	standard	standard
standard	standard	standard	standard	standard	standard	standard	standard
Asymmetric	Asymmetric	Asymmetric	Asymmetric	Asymmetric	Asymmetric	Asymmetric	Asymmetric
1.2	1.2	1.2	1.2	1.2	1.2	1.2	1.2
r&i r	r&i r	r&i r	r&i r	r&i r	r&i r	r&i r	r&i r
1	1	1	1	1	1	1	1
1.5	1.5	1.5	1.5	1.5	1.5	1.5	1.5
2.5	2.5	2.5	2.5	2.5	2.5	2.5	2.5
5	5	5	5	5	5	5	5
2-6	2-6	2-6	2-6	2-6	2-6	2-6	2-6
10000	10	10	10	10	10	10	10
8	12	8	8	8	8	8	8
2	2	1	3	2	2	2	2
-	-	-	-	r&i r	-	-	-
-	-	-	-	3	-	-	-
-	-	-	-	2	-	-	-
-	-	-	-	3	-	-	-
-	-	-	-	-	Simple Avg	Simple Avg	
-	-	-	-	-	6	6	
-	-	-	-	-	-	1	
-	-	-	-	-	-	-	
-	-	-	-	-	-	-	
-	-	-	-	-	-	-	
-	-	-	-	-	-	-	

	P0034 PIV+PTV	P0035 PIV+PTV	P0036 PIV+PTV
-	-	-	-
-	-	-	-
64	64	64	64
square	square	square	square
50	50	50	50
2	2	2	2
32	32	32	32
square	square	square	square
75	75	75	75
2	2	2	2
N	N	N	N
-	-	-	-
standard	standard	standard	standard
standard	standard	standard	standard
Asymmetric	Asymmetric	Asymmetric	Asymmetric
1.2	1.2	1.2	1.2
r&i r	r&i r	r&i r	r&i r
1	1	1	1
1.5	1.5	1.5	1.5
2.5	2.5	2.5	2.5
5	5	5	5
2-6	2-6	2-6	2-6
10	10	10	10
8	8	8	8
2	2	2	2
-	-	-	-
-	-	-	-
-	-	-	-
-	-	-	-
Poly2			
6	-	-	-
-	-	-	-
-	Simple Avg		Poly2
-	6	6	6
-	8	8	8
-	8	8	8